NASA/CR- 94- 207343

Radiative Energy Budget Studies using Observations from the Earth Radiation Budget Experiment (ERBE) (Final Report for NASA grant NAGW-3935)

Dr. Steven A. Ackerman
Principal Investigator

Contributing authors:
R. Frey
M. Shie
R. Olson
C. Collimore
M. Friedman

1

Table of Contents

Introduction

Our research activities under this NASA grant have focused on two broad topics associated with the Earth Radiation Budget Experiment (ERBE):

- The role of clouds and the surface in modifying the radiative balance.
- The spatial and temporal variability of the earth's radiation budget

Each of these broad topics is discussed separately in the text that follows. The grant supported three graduate students, Ms. Mei-Guei Shie (full support), Mr. Erik Olson (partial support) and Mr. Michael Friedman (partial support). Ms. Shie will be graduate with a master's degree in May 1998. The major points of her thesis are summarized in section 3 of this report. Her complete thesis "Diurnal variabilities of Radiation Properties over the Amazon with Applications on Ecosystems and Biomass Burning" will be available in May 1998 and is available on request. Mr. Erik Olson is working on a Ph.D.; his contributions are summarized in section 3. Mr. Friedman will complete his Ph.D. work in August 1998. His dissertation focuses on deriving the radiation budget over the TOGA COARE region.

The grant supported in the following publications.

Ackerman, S. A., 1997: Remote sensing aerosols from satellite infrared observations. *J. Geo. Res.*, **102**, 17069-17079.

Frey, R. A., S. A. Ackerman, and B. J. Soden, 1995: Climate parameters from satellite spectral measurements. Part I: Collocated AVHRR and HIRS/2 observations of the spectral greenhouse parameter. *Jour. Clim.* **9**, 327-344.

Ackerman, S. A., 1996: Monitoring the Antarctic radiation inversion using satellite measurements at 11 and 6.7 μm. International Radiation Symposium, August, Fairbanks Alaska. (refereed)

Ackerman, S. A., 1996: Remote sensing aerosols from IR satellite observations. Aerosol Remote Sensing Workshop. April 15-19, Washington D.C.

Moeller, C., S. A. Ackerman, K. I. Strabala, W. P. Menzel and W. L. Smith, 1996: Negative 11 micron minus 12 micron brightness temperature differences: A second look. Eighth Conference on Satellite Meteorology and Oceanography.

Ackerman, S. A. and R. A. Frey, 1995: Climate parameters from collocated AVHRR and HIRS/2 observations: Clear-sky spectral greenhouse parameter. AMS Sixth Symposium on Global Change Studies. Dallas, Tx. 15-20 January.

Papers in preparation include:

Ackerman, S. A., and R. A. Frey, 1998: Climate parameters from satellite spectral measurements. Part II: Collocated AVHRR and HIRS/2 observations of the spectral cloud forcing. *Jour. Clim.*

Inoue, T., and S. A. Ackerman, 1998: Radiative energy budget over the eastern Pacific Ocean using collocated AVHRR and ERBE observations, *Jour. Appl. Met.*

This report focuses on material that has not yet been published.

The role of clouds and the surface in modifying the radiative budget.

One of our approaches to studying the effects of clouds and the surface on the radiation budget of the planet, is to collocate AVHRR and ERBE observations. The collocation procedure has been published (Ackerman and Inoue, 1994; Ackerman et al., 1992). Through collocation of the AVHRR data we can better define the state of the atmosphere and the surface within the ERBE field-of-view (FOV). For example, the AVHRR observations are analyzed to determine clear-sky ERBE FOV and to define surface vegetation indices. The AVHRR data are also used to determine the predominate cloud type within the ERBE FOV.

Cloud Properties

Broadband studies

We have worked with Dr. T. Inoue of Japan to study the broadband radiative properties of different cloud types using collocated AVHRR and ERBE data. Cloud detection This study makes use of collocated AVHRR and ERBE observations made from the NOAA-9 polar orbiting satellite, over the eastern Pacific for the years 1985 and 1986. The NOAA-9 nominal equator crossing times are 0900 UTC and 2100 UTC.

The AVHRR data used in this study is the Global Area Coverage (GAC) data which has a nominal resolution at nadir of 4 km. The AVHRR has 5 spectral bandpasses: Channel 1 (0.56-0.68 μm); Channel 2 (.725-1.1 μm); Channel 3 (3.55-3.93 μm); Channel 4 (10.3-11.3 μm); and Channel 5 (11.5-12.5 μm). These 5 channels are located in spectral regions where atmospheric gases are characterized by weak absorption. The AVHRR data are therefore good for studying surface properties, such as sea surface temperature and vegetation properties, and cloud top properties. Inoue (1987) developed a cloud type classification, referred to as the split window technique, based on the equivalent brightness temperature in Channel 4 (BT $_{11}$) and the temperature difference between Channel 4 and 5 (DBT). This classification scheme is adopted in the present study.

ERBE observations are used to specify the broadband energy budget at the top of the atmosphere. At nadir the ERBE footprint is approximate 35 km. The ERBE scanning instrument has been discussed by Kopia (1986). The method of inverting the instantaneous scanner observations to the top of the atmosphere fluxes is discussed in Barkstrom et al. (1989), and Smith et al. (1986).

Collocation of the AVHRR pixels with the ERBE footprint is accomplished based on the method developed by Ackerman et al. (1992) and Ackerman and Inoue (1995). The method is based on the scanning geometry of both instruments.

Data Analysis

Figure 1 depicts the split window classification scheme. The first step is to determine the clear-sky thresholds BT $_{11}$ and DBT for each ERBE 2.5x2.5 latitude longitude region within the area of study. This is accomplished through analyze of 3x3 groups of AVHRR pixels that lie within each ERBE footprint. In Step 1, a first guess threshold of BT $_{11}$ is determined using the spatial coherence approach of Coakley and Bretherton (1987). The spatial coherence method is used to estimate the clear-sky

2

thresholds for BT $_{11}$, specified as the foot of the "foot" of the clear-sky arch. The 3 ×3 groups of pixels are then re-analyzed.
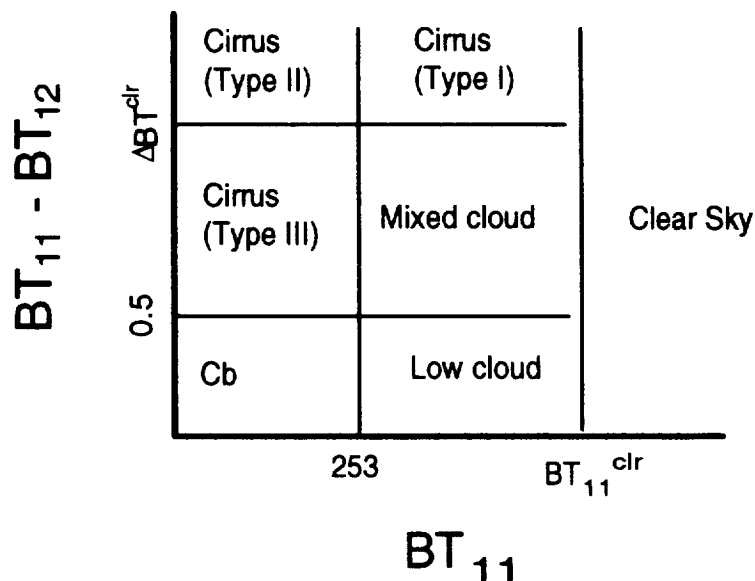

Figure 1. Split window classification of Inoue (1987).

In the second pass through the data, only those groups of nine pixels that have a standard deviation less than 0.4C and a mean BT $_{11}$ that is greater than the initial threshold selected by the spatial coherence analysis are considered. Each group of AVHRR pixels is assigned an appropriate ERBE 2.5 by 2.5 degree grid box. The mean BT $_{11}$ and mean ΔBT for each ERBE grid box are then computed and assigned the clear-sky threshold values.

Having selected a clear-sky threshold that is a function of month and geographic region, a third pass through the data is made. In this final pass, each individual AVHRR pixel that lies within and ERBE footprint is classified according to the split window technique.

To compute the regression equation that transforms the AVHRR observations to longwave (LW) fluxes, only ERBE footprints with uniform split window classifications are used. In other words, in the clear-sky regression only ERBE footprints in which all the AVHRR pixels are classified as clear are used. Data from January, April, July and October are used in the least square fitting.

Figure 2 depicts the relationship between the ERBE LW and shortwave(SW) fluxes categorized by the split window classification. For this region the split window selects primarily clear, low cloud, mixed scene, cirrus (Type I) and cumulonimbus. The fluxes associated with these classifications are consistent with expectations. Cumulonimbus clouds have a low LW flux and a large shortwave flux. Clear-skies exhibit low SW fluxes and warm temperatures. Cirrus and low clouds also separate out on this figure, both have similar LW fluxes but the cirrus have a much smaller SW flux.
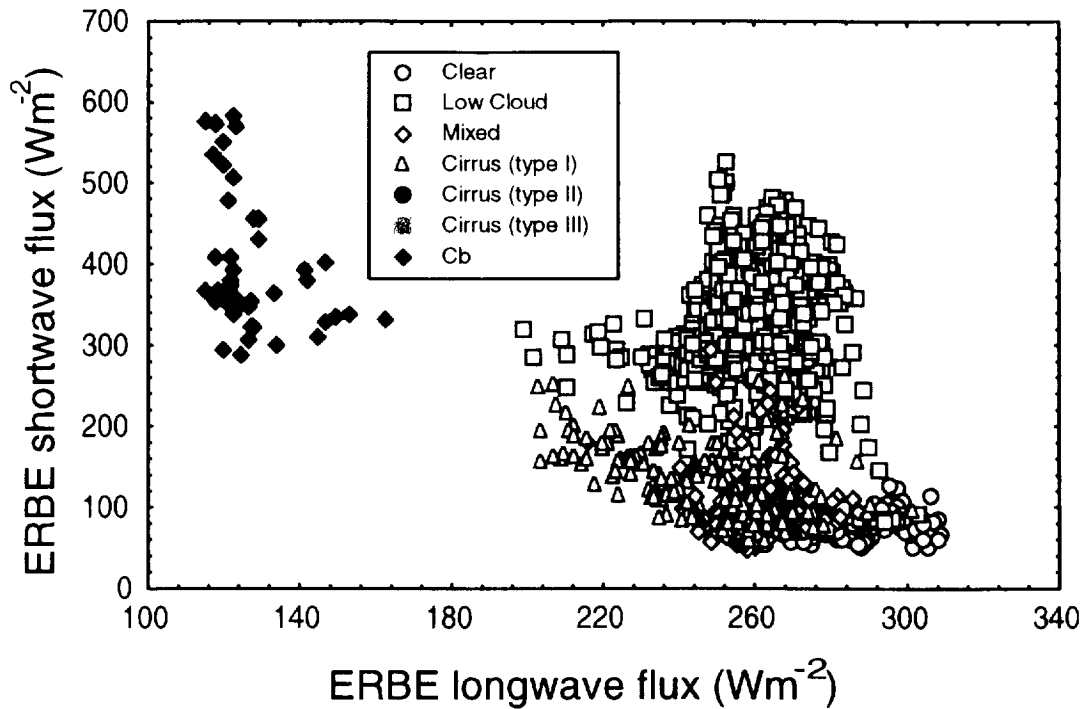
3

Figure 2. Relationship between ERBE LW and SW fluxes as a function of cloud type.

Separate coefficients are derived for each of the seven split window scenes classifications. The predicted LW fluxes using the regions versus ERBE observed fluxes are shown in Figure 3. The need to separate the regressions as a function of cloud type results as different relationships exist between the window brightness temperature and the broadband flux. This is particularly evident in the low cloud and cirrus cases; similar BT_{11} for these two clouds yield different LW fluxes. Also, the relationship between the broadband flux and window channel observation for the low cloud is different from the clear sky regression. The role of the split window in the regression varies with the scene type. In the clear sky cases the split window becomes an estimate, or correction, for the water vapor effects. In the cloud case it represents an integrated water amount and the combined effect of cloud optical thickness and microphysical properties. For the clear sky cases the split window improves the regression by lowering the standard error from 10 to 6. For the cirrus clouds it has little impact on the regression. However, the importance of the split window is in the classifications. If the scene is not classified and regression carried out on all the data the standard error is 20 Wm^{-2}. A regression on all scene using the window channel alone yields a standard error of more than 40 Wm^{-2}.

The regressions derived from the uniform scenes are now applied to the all the ERBE observations. Each AVHRR pixel within the ERBE footprint is classified according to the split window classification. The appropriate regression is applied to each individual pixel. The total flux is then derived by linear weighting the fluxes of each pixel lying within the ERBE footprint. Figure 3 depicts the predicted versus observed LW flux. A histogram of the difference between the predicted and observed flux is shown in Figure 4. There is a bias, 5 W m^{-2} in the predicted flux. Most of the predicted fluxes, approximately 80%, lie within 10 Wm^{-2} of the observed flux. Footprints that have a large difference between the observed and predicted flux are associated with very

4

non-uniform fields-of-view, standard deviation of greater than 5C. There are two reasons for this. The first is that the linear weighting cloud amount may be inappropriate. The second is that the ERBE scanner has a point spread function that is not accounted for in the linear weighed average.

With this fitting procedure, we could now calculate the cloud forcing as a function of cloud fraction within the ERBE footprint, where the clear-sky value is based on the regression fit of AVHRR versus ERBE clear-sky footprints. The results are depicted in Figure 5. The average change in LW cloud forcing is approximately 0.15 Wm-2 per 1% change in cloud fraction. Of course this is a function of cloud type (Figure 6). The collocated files allow us to determine the cloud forcing as a function of cloud fraction as a function of cloud type.
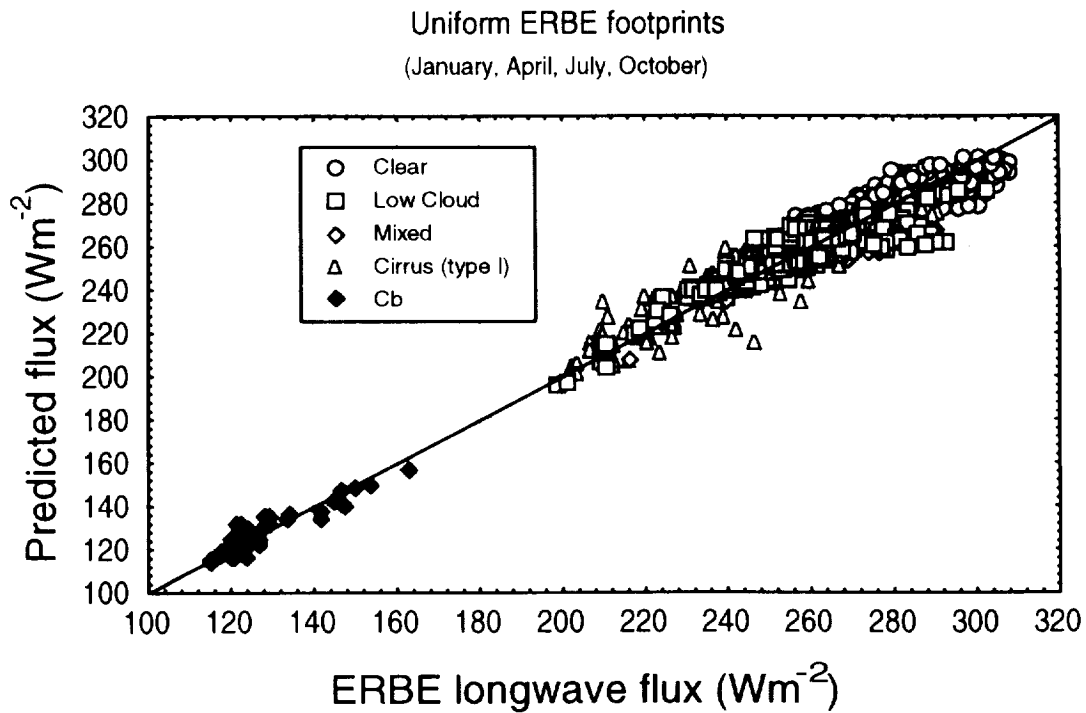

Figure 3. ERBE observed OLR as a function of predicted flux from regression.
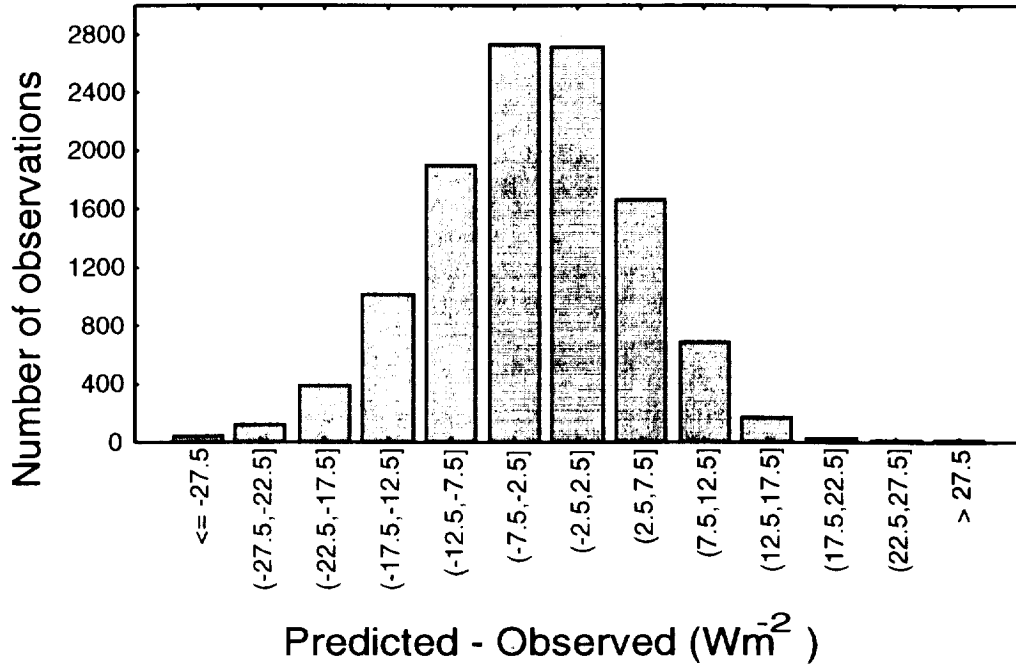
Figure 4 (chart)

Y-axis: Number of observations — 0, 400, 800, 1200, 1600, 2000, 2400, 2800

X-axis categories: <= -27.5, (-27.5,-22.5], (-22.5,-17.5], (-17.5,-12.5], (-12.5,-7.5], (-7.5,-2.5], (-2.5,2.5], (2.5,7.5], (7.5,12.5], (12.5,17.5], (17.5,22.5], (22.5,27.5], > 27.5

X-axis label: Predicted - Observed (Wm^{-2})

Figure 4. Histogram of the difference in predicted and observed OLR using uniform and non-uniform scenes.

Figure 5 (chart)

Y-axis: LW cloud forcing (Wm^{-2}) — -20, 0, 20, 40, 60, 80, 100, 120, 140, 160, 180, 200

Legend:
- Non-Outlier Max
- Non-Outlier Min
- 75%
- 25%
- Median
- Outliers
- Extremes

$$\frac{\Delta LW}{\Delta \%} = 0.15\ W\ m^{-2}\%^{-1}$$

X-axis categories: <= 10, (10,20], (20,30], (30,40], (40,50], (50,60], (60,70], (70,80], (80,90], > 90

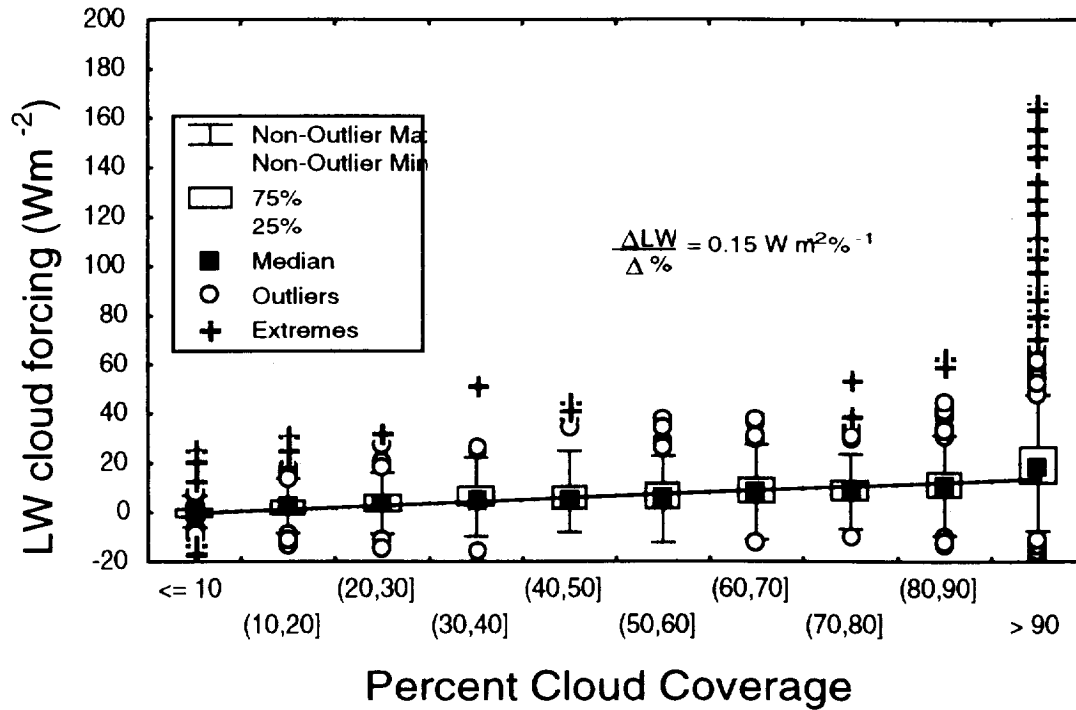X-axis label: Percent Cloud Coverage

Figure 5. LW cloud forcing as a function of cloud coverage from collocated ERBE and AVHRR data.
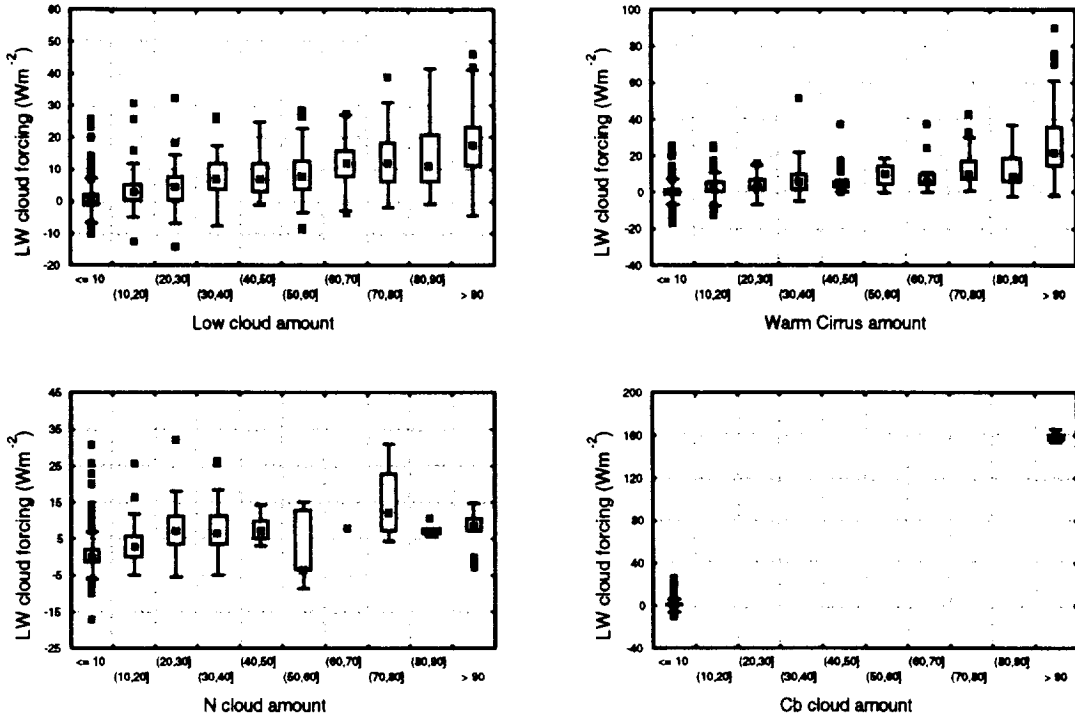
6

Figure 6. LW Cloud forcing as a function of cloud amount for four different cloud types.

Spectral studies

Spectral cloud forcing was also investigated under this grant using collocated HIRS/2 and AVHRR observations. The analysis of the data is based on the Collocated HIRS/2 and AVHRR Processing Scheme (CHAPS) described by Frey et al, (1996).

Clear and Cloudy Scene Discrimination and Confidence Levels

The first step in any cloud radiative forcing scheme is to discriminate between clear and cloudy-sky scenes. The CHAPS algorithm makes use of radiance data at three spatial scales in order to make this determination for regions defined by HIRS/2 fields of view (FOVs): HIRS single-footprint data (17 km resolution at nadir), AVHRR Global Area Coverage (GAC) measurements at 4 km nominal resolution, and AVHRR histograms over regions approximately 280 km on a side. We will henceforth use FOV to mean a single HIRS/2 footprint as well as all collocated AVHRR footprints (referred to as pixels) which fit inside it. Collocated pixel data will refer to AVHRR measurements which are located within specific HIRS/2 footprints. Histograms of AVHRR collocated pixel data are collected over ISCCP (International Satellite Cloud Climatology Project) $2.5°$ latitude equal-surface-area regions (Rossow and Schiffer, 1991). Spectral clear-sky tests use single HIRS/2 measurements along with corresponding collocated mean AVHRR radiance data. The histograms are used for the purpose of deriving representative 11 µm clear-sky brightness temperatures (T_b) for ISCCP gridboxes. Spatial variability in FOVs is estimated using the AVHRR values found within them.

Table 1 lists the clear-sky tests used for ocean regions. The method is fully described in Frey et al., (1995).

If all the clear-sky tests are passed for a given FOV, then we label it a "high-confidence clear-sky scene". Conversely, if any test is failed, then the FOV is tentatively called "cloudy". The intent is to flag all data where it is highly likely that the entire FOV is clear. Since this also implies that all the collocated AVHRR observations come from clear-sky conditions, one additional check is performed on all FOVs initially labeled clear. A sea-surface temperature (SST) estimate is calculated from the mean collocated AVHRR 11 and 12 μm T_bs using the NOAA operational technique (McClain, 1989; Wade, 1993). If the AVHRR-derived SST is colder than the value in the Reynolds' blended SST data set by more than 6 $^\circ K$, then the FOV is still labeled clear, but is given lowered confidence since we have no way to determine which SST is more correct.

The cloudy FOVs are then checked for consistency. All the collocated AVHRR 11 μm T_bs in each FOV are compared with their respective regional clear-sky thresholds. These thresholds are calculated from all collocated AVHRR 11 μm T_bs in an ISCCP region which satisfy some initial gross clear-sky requirements (Frey et al., 1995). This is the same threshold mentioned above. If all the AVHRR T $_b$s in a FOV are greater than the clear-sky threshold, then the FOV is said to be clear, but with lowered confidence.

All remaining cloudy FOVs are sorted into one of six possible categories - low, middle, or high clouds - with either high or lowered confidences. These classifications apply to the entire FOV and are based on cloud pressure altitude determined by the CO_2-slicing algorithm (Smith et al, 1974; Smith, 1978; Menzel et al, 1983) using HIRS/2 radiance data, and spatial variability computed from collocated AVHRR 11 μm T_bs.

Table 1 CHAPS Spectral Clear-sky Tests

- If daytime, mean collocated AVHRR NIR reflectance $\leq 6.5\%$
- Mean collocated AVHRR 11 μm $T_{bb} \geq$ clear-sky threshold
- Collocated AVHRR 3.7 μm standard deviation $\leq 0.5K$
- Collocated AVHRR 11 μm standard deviation $\leq 0.5K$
- HIRS/2 8-11 μm T_{bb} difference $< -3.5K$
- Mean collocated AVHRR 11-12 μm T_{bb} difference $> 0.5K$
- CO_2-slicing cloud height > 500 mb

8

Total Cloud Cover

Figure 7 depicts the CHAPS derived January and July 1994 total cloud cover determined using the AVHRR pixels, for the region 60 °N to 60°S. Global cloud features are captured, including the marine stratus regions, tropical convection zones and midlatitude winter storm tracks. ISCCP is internationally recognized algorithm for retrieving cloud from satellite observations. The ISCCP cloud-detection algorithm consists of five steps (Rossow and Garder 1993): (1) space contrast test on a single infrared image; (2) time contrast test on three consecutive infrared images at constant diurnal phase; (3) cumulating space/time statistics for infrared and visible images; (4) construction of clear-sky composites for infrared and visible every 5 days at each diurnal phase and location; and (5) radiance threshold for infrared and visible for each pixel. While the 1994 data have not bee processed, we compare the CHAPS derived cloud cover with the ISCCP mean cloud cover.

Figure 8 plots the differences in cloud amount derived from the CHAPS and ISCCP algorithms. While the sampling times of the two algorithms are different, this figure demonstrates the tendency of CHAPS to retrieve greater cloud amount than ISCCP. This is expected as the CHAPS algorithm is clear-sky conservative as its focus is to derive high confident clear HIRS/2 footprint scenes. On the other hand, the ISCCP algorithm is constructed to be cloud-conservative, it minimizes false cloud detection but misses clouds that resemble clear conditions. ISCCP retrieves less clouds than CHAPS in the 30°-60°S latitude belt in both months. CHAPS also retrieves more cloud than ISCCP poleward of 30°N in July.

9

January 1994 CHAPS Cloud Amount (%)
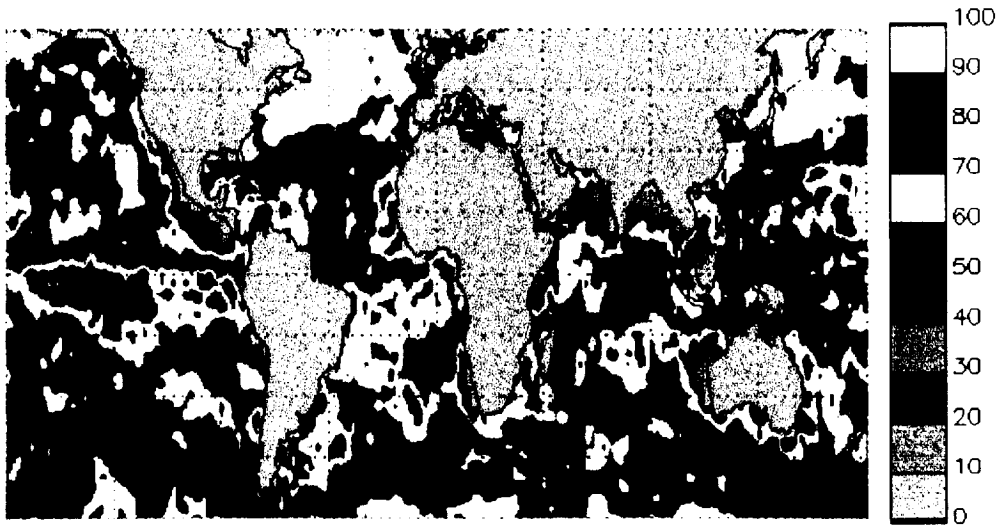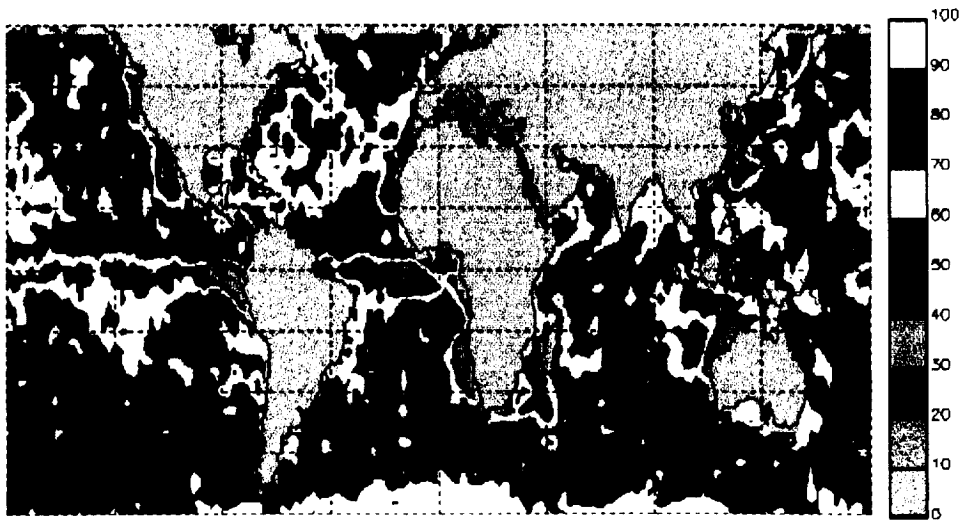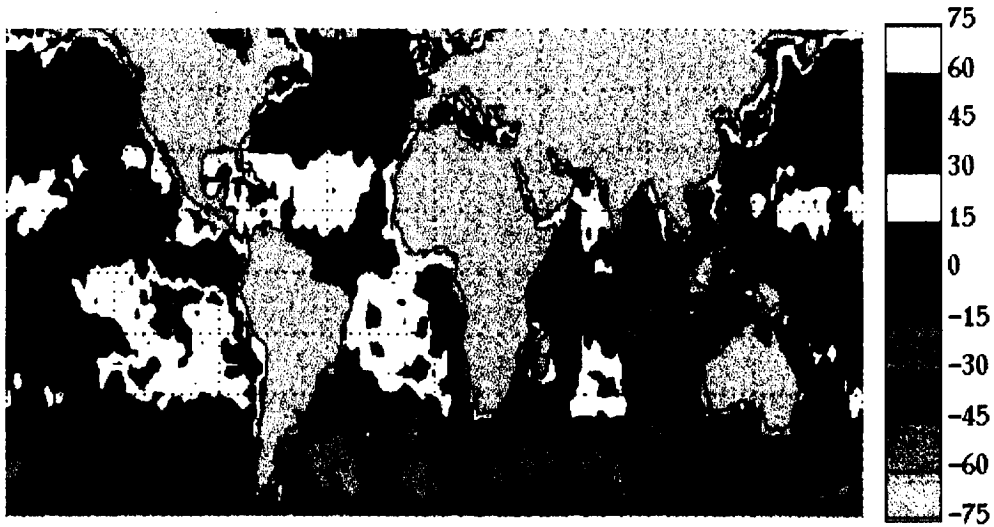

July 1994 CHAPS Cloud Amount (%)

Figure 7. Cloud amount derived from AVHRR pixel for January 1994 and July 1994.

January 1994 CHAPS-ISCPP Cloud Amount (%)

July 1994 CHAPS-ISCCP Cloud Amount Difference (%)

Figure 8. Difference in cloud amount derived from CHAPS and ISCCP January 1994 and July.

CO_2-slicing Algorithm as Implemented in CHAPS Processing

CHAPS algorithm for retrieving cloud altitudes is determined as in Menzel *et al.* (1983), except that spectral clear-sky radiances are computed rather than taken from observations. Time and space-interpolated temperature and moisture profiles from the National Meteorological Center (NMC) forecast model output are used in the radiative transfer calculations. There are several advantages to be gained by using simulated radiances in automated global processing. Only one pass through the data is required, reducing the amount of computer time needed. Also, some parts of the world are extremely cloudy during certain seasons or times of day and therefore have little chance of being observed during clear weather conditions. For these regions, interpolation of observations from differing times or places is less likely to yield accurate clear-sky radiative characteristics. Of course, the limitation on the computational method is the accuracy of the input profile data. To reduce systematic biases from being introduced into the cloud height calculations, simulated HIRS/2 spectral radiances from clear-sky FOVs were compared to the corresponding observed radiances for several days at the beginning of each month processed. A regression relationship was then developed for a correction to the simulated radiances during subsequent reprocessing of the data. One relationship was derived for all ocean regions. (In a continuous operational setting, this could be done automatically, with the radiances stored in a rotating file containing data from several previous days.)

Tables 2 and 3 show January 1994 global oceanic cloud altitude and effective emissivity statistics from Wylie et al. (1994) and CHAPS, respectively. The effective emissivity may be thought of as a combination of the fractional cloud amount and cloud emissivity in the FOVs. The tables show remarkably similar results. The major differences are in the amount of clear sky (CHAPS finds about 2.5% more), clouds at levels higher than 400 mb which have > 95% effective emissivity (CHAPS finds about 2.5% less), and in the amount of clouds found between 700 and 799 mb (CHAPS finds about 5% more). The latter discrepancy can be traced to the sixth column of the tables which shows the frequency of opaque clouds. Please note that in this context "clear sky" refers to a retrieved cloud altitude of ≥ 1000 mb and not to the result of the full CHAPS algorithm.

Regional differences between the two data sets are detailed in Figures 9 and 10, which show monthly oceanic high cloud frequencies for January and July of 1994. The spatial distributions are very similar, with the highest frequencies of high altitude clouds found mostly in tropical areas. But this is also where the most of the larger differences occur in an absolute sense. As shown in Figures 9 and 10, frequencies in the world's convective and stormy mid-latitude regions differ by as much as 60%, while those in areas characterized by atmospheric subsidence agree quite well. These discrepancies could be caused by large differences between the clear-sky radiances used by the two different algorithms. Since polar orbiting satellites take measurements only twice daily over any particular spot, it can be difficult to obtain clear-sky observations in very cloudy regions. If radiances from adjacent sub-tropics are consistently used in place of those from the tropics or mid-latitudes, those generally warmer values from mid-atmospheric sounding channels could lead to errors in monthly mean cloud heights and amounts. It is also worth noting the sampling rate difference between the two products. The CHAPS procedure analyzes the middle 28 FOVs of each HIRS scan line, while only three FOVs on every third scan line are processed by

12

the Wylie method. While this leads to a smoother-looking CHAPS image, we would not expect it to lead to the large differences seen in parts of Figures 9 and 10.

13

Table 2. Wylie-Menzel CO$_2$-slicing results for ocean regions in January 1994.

Wylie-Menzel CO$_2$-slicing Results for January 1994 Values are Percent of Total					
Effective Emissivity (%)					
Level (mb)	< 25%	< 50%	< 75%	< 95%	> 95%	All Obs
100-199	2.19	0.70	0.36	0.89	0.66	4.81
200-299	3.34	2.30	1.83	2.67	1.69	11.84
300-399	3.51	2.64	2.66	2.75	1.09	12.65
400-499	2.94	2.79	2.91	2.58	0.46	11.69
500-599	1.58	2.58	2.89	0.84	0.63	8.53
600-699	0.65	1.28	2.01	0.83	2.37	7.14
700-799	0.14	0.37	0.46	0.06	5.10	6.14
800-899	0.00	0.00	0.00	0.00	9.20	9.20
900-999	0.00	0.00	0.00	0.00	8.13	8.13
Clear-sky	19.88	0.00	0.00	0.00	0.00	19.88
Totals	34.22	12.68	13.14	10.62	29.34	100.00

Table 3 CHAPS CO$_2$-slicing results for ocean regions in January 1994.

CHAPS CO$_2$-slicing Results for January 1994 Values are Percent of Total					
Effective Emissivity (%)					
Level (mb)	< 25%	< 50%	< 75%	< 95%	> 95%	All Obs
100-199	2.72	0.52	0.18	1.58	0.21	5.21
200-299	3.39	1.99	1.42	3.10	0.13	10.02
300-399	2.82	2.12	2.21	3.14	0.45	10.74
400-499	1.90	2.26	2.48	3.07	0.48	10.18
500-599	0.88	1.97	2.30	0.97	0.68	6.80
600-699	0.30	0.99	1.53	0.84	2.45	6.02
700-799	0.08	0.49	0.57	0.09	9.29	10.53
800-899	0.00	0.05	0.02	0.00	9.33	9.41
900-999	0.00	0.00	0.01	0.00	8.78	8.80
Clear-sky	21.58	0.00	0.00	0.00	0.71	22.29
Totals	33.69	10.39	10.71	12.70	32.51	100.00

14
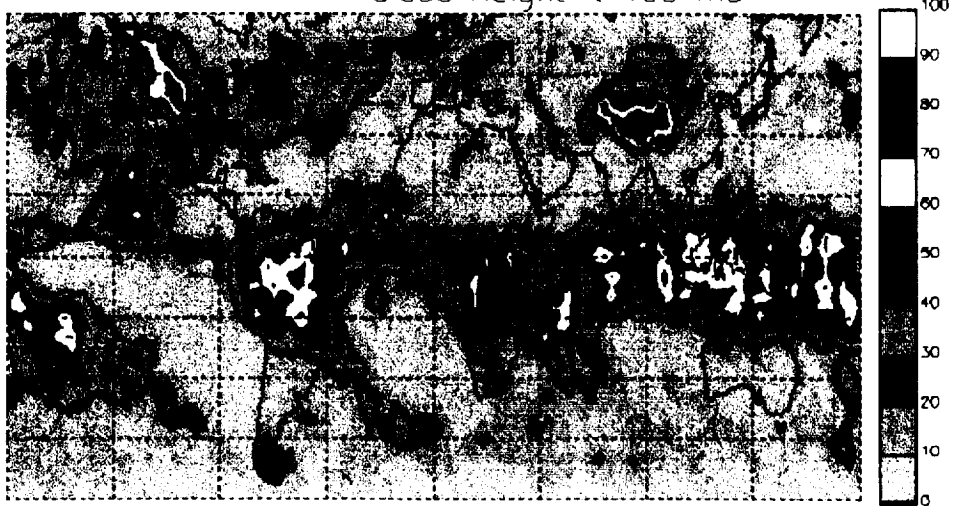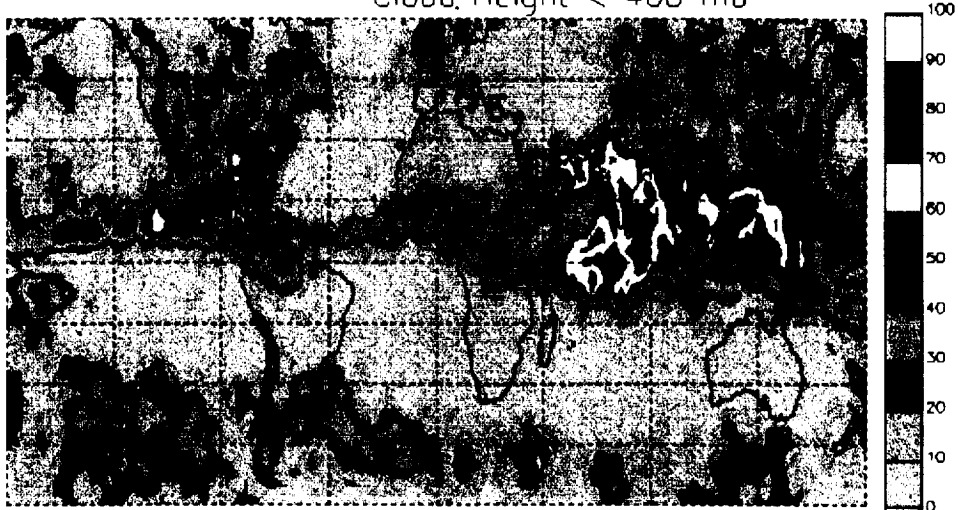
Figure 9. CHAPS derived high cloud frequency for January and July 1994.

Figure 10. Wylie-Menzel high cloud frequency for January and July 1994.

16

The comparisons of CHAPS with the Menzel demonstrate that CHAPS is clear-sky conservative. For the remainder of this study, high clouds are defined as those with computed cloud pressure altitudes of 300 mb or less, those greater than 300 mb but less than or equal to 600 mb are labeled as mid-level, and those greater than 600 mb are categorized as low clouds. Retrieval confidences are based on FOV standard deviations as a function of mean FOV AVHRR T_bs computed from collocated 11 μm AVHRR pixel data. Cloudy FOVs are labeled "high-confidence" if their standard deviations are below a threshold which ranges linearly from 1.5 °K at 280°K and above to 6°K at 210°K and below. An additional requirement for high-confidence high clouds is a HIRS/2 8.2–11 μm difference greater than 0 °K.

Clear and cloudy-sky HIRS/2 radiances were collected over each of the three months processed (here we only show January and July 1994), where "clear" means "high-confidence clear" as defined above and "cloudy" refers to all other observations. Single-FOV values were sorted into 2.5 ° latitude/longitude bins according to the ERBE (Earth Radiation Budget Experiment) gridding system (ERBE Data Management Team, 1991). Monthly means of both clear and cloudy-sky radiances were generated for each ERBE gridbox where possible.

Broadband Cloud Radiative Forcing

Before investigating the spectral cloud forcing it is instructive to view the broadband OLR using the CHAPS data. To do this, the algorithm of Ellingson (personel communication) is used to convert the spectral channels to a broadband flux using a least square algorithm. Figure 11 shows the January and July 1994 OLR derived from the CHAPS data set. This is similar to the ERBE monthly mean OLR. Broadband cloud forcing was also derived using the CHAPS data and is shown in Figure 12. The CHAPS data set does not overlap with the ERBE scanner data and therefore a direct comparison cannot be performed, only trends.

The geographic distributions of the longwave cloud forcing are similar to that described by the ERBE data (Harrison et al, Ramanathan et al 1989). The CHAPS broadband cloud forcing for the subtropical high pressure regions is similar to that of ERBE, being less than 20 Wm^{-2}. In the tropical convective regions, CHAPS tends to have lower values than ERBE. CHAPS is more restrictive in deriving clear-sky conditions, and thus has more missing data regions than ERBE.
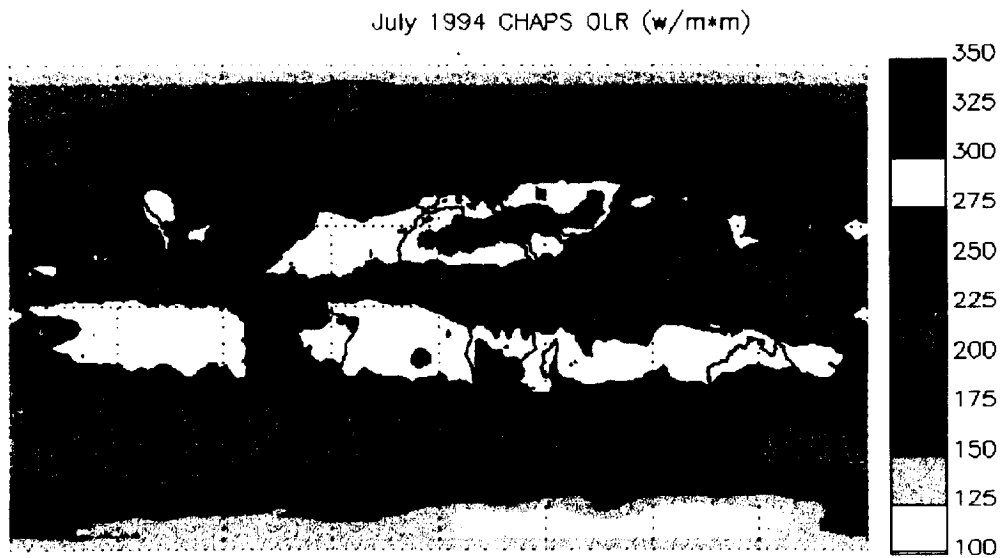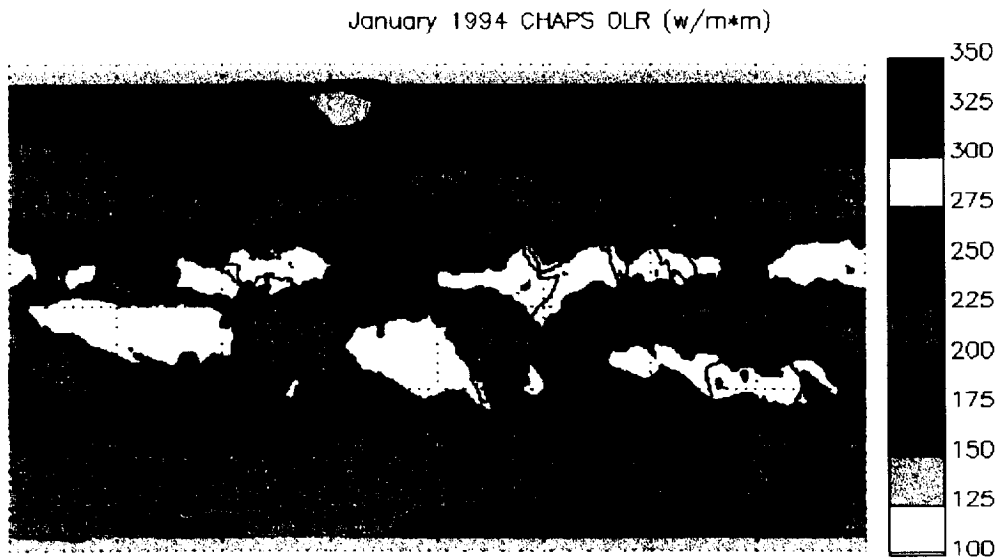
17

January 1994 CHAPS OLR (w/m*m)

July 1994 CHAPS OLR (w/m*m)

Figure 11. Broadband outgoing longwave radiation derived from the CHAPS data set.

18

January 1994 CHAPS Broadband Cloud Forcing (w/m*m)


July 1994 CHAPS Broadband Cloud Forcing (w/m*m)

Figure 11. Broadband longwave cloud forcing derived from the CHAPS data set.

Spectral Cloud Radiative Forcing

Using blackbody temperatures corresponding to these radiances, channel flux densities were computed for the HIRS/2 6.7, 7.3, 8.2, and 11.1 μm spectral bandpasses (response functions). The limits of integration were defined as the half-power points of each channel. The spectral cloud radiative forcing was then defined as the difference between the clear-sky and cloudy-sky channel flux densities in each of the above bands for each ERBE gridbox which had both clear and cloudy-sky values.

Figures 13 and 14 display the derived spectral cloud forcing at 6.7, 7.3, 8.2, and 11.1 μm for January and July 1994, respectively. The spectral cloud forcing is a function of clear sky radiance, cloud amount and cloud type. Thus, there is a seasonal and geographic dependence. Middle latitude storm tracks and tropical convection are clearly evident in these figures. The 8.2 and 11 μm channels have the largest spectral forcing because the atmospheric transmittance is smaller at these channels that at 6.7 and 7.3 μm. Convective regions have the largest spectral forcing. Stratus regions have minimal impact on the 6.7 and 7.3 μm spectral cloud forcing. Thus, clouds modify the top of atmosphere spectral distribution of energy.

January 1994 CHAPS 6.7 μm Spectral Cloud Forcing
× 100
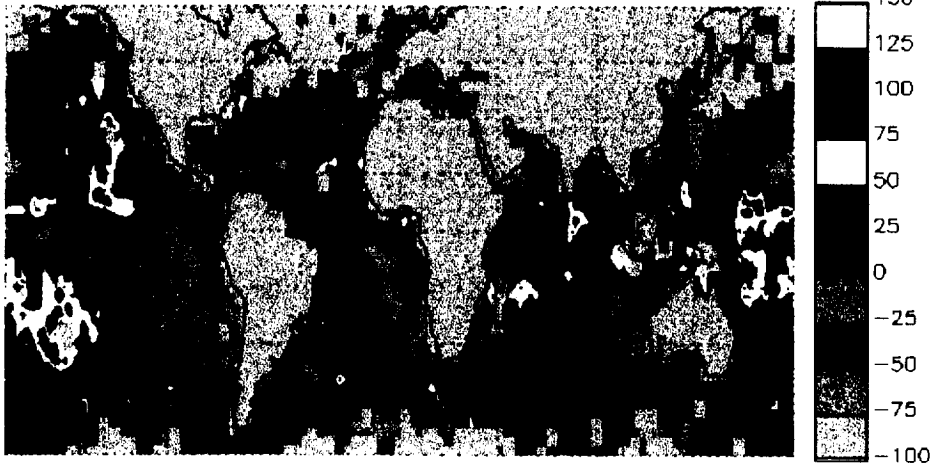
January 1994 CHAPS 7.3 μm Spectral Cloud Forcing
× 100

21
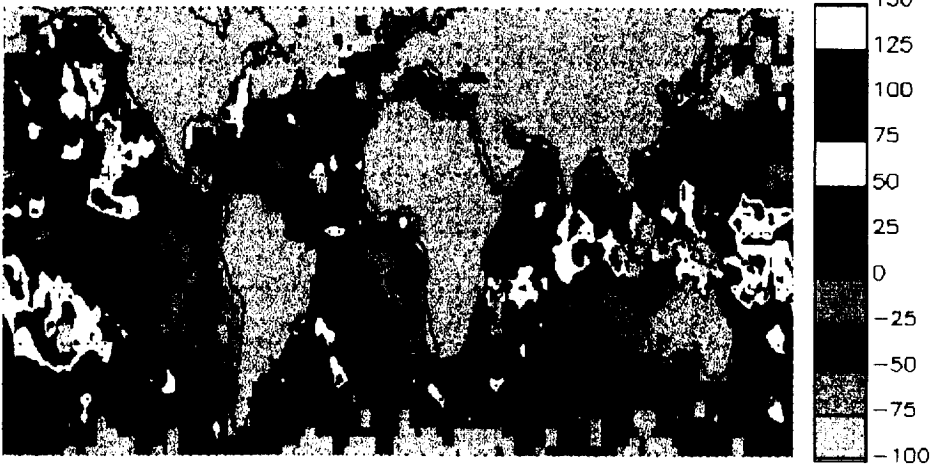
January 1994 CHAPS 8.2 μm Spectral Cloud Forcing

January 1994 CHAPS 11 μm Spectral Cloud Forcing

Figure 13. January 1994 spectral cloud forcing over oceans for the 6.7, 7.2, 8.3 and 11 μm channels of the HIRS/2.

22

July 1994 CHAPS 6.7 μm Spectral Cloud Forcing
× 100

150
125
100
75
50
25
0
−25
−50
−75
−100

July 1994 CHAPS 7.3 μm Spectral Cloud Forcing
× 100

150
125
100
75
50
25
0
−25
−50
−75
−100

23

July 1994 CHAPS 8.2 μm Spectral Cloud Forcing

July 1994 CHAPS 11 μm Spectral Cloud Forcing

Figure 14. July 1994 spectral cloud forcing over oceans for the 6.7, 7.2, 8.3 and 11 μm channels of the HIRS/2.

Histograms of the monthly average July 1994 spectral cloud forcing for 0-15 North and 30-45S latitude are shown in Figure 15 and 16 respectively. Each spectral cloud forcing is categorized as a function of effective cloud amount (determined from the CO_2 slicing). This histograms indicate how clouds effect the spectral distribution of energy at the top-of-atmosphere. As expected the 8.2 and 11 μm regions have the greatest spectral cloud forcing. The large the effective cloud amount (η) the larger the forcing. The dependence on effective cloud amount is a function of wavelength. For example, the 14.2 micron channel the spectral cloud forcing is nearly the same for $\eta > 75\%$ as it is for η between 25 and 75%, while the 8.2 and 11 micron channels show a much stronger dependence on η.

24

CHAPS Spectral Cloud Forcing
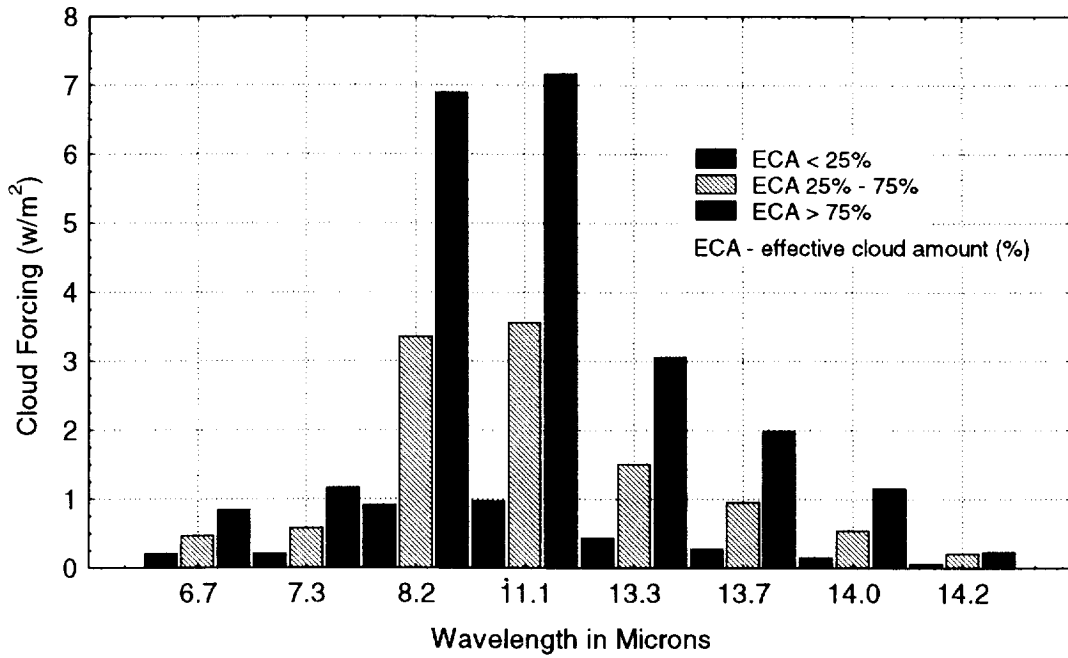Monthly 0-15 North Latitude Mean from July 1994

Figure 15. Histogram of spectral cloud forcing for different effective cloud amounts for the ocean regions between 0-15 N, in July 1994.

CHAPS Spectral Cloud Forcing
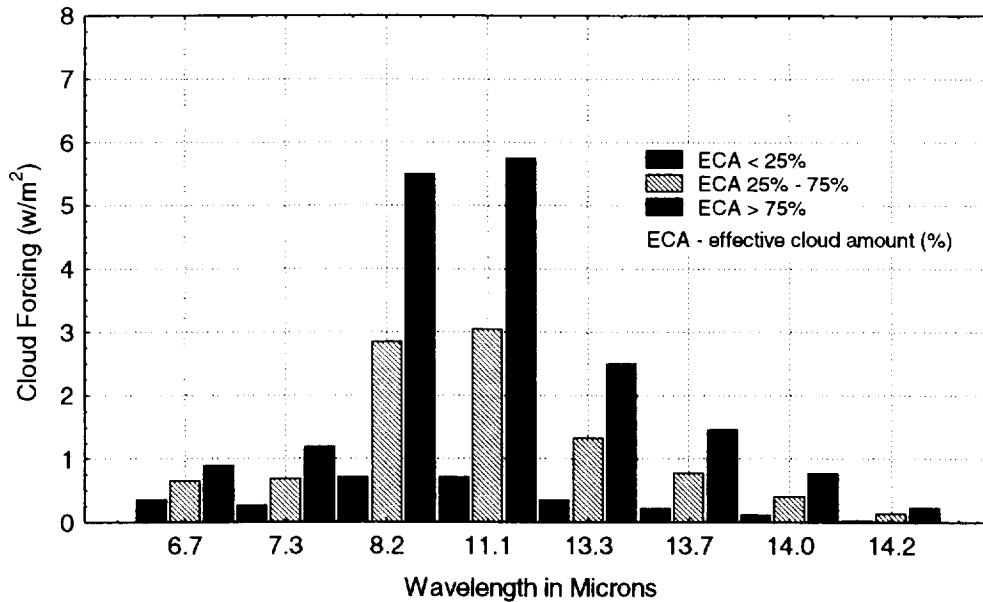Monthly 30-45 South Latitude Mean from July 1994

Figure 16. Histogram of spectral cloud forcing for different effective cloud amounts for the ocean regions between 30-45 S, in July 1994.

The spectral cloud forcing is also a function of cloud type. This is demonstrated in Figures 17 and 18. In these figures the spectral cloud forcing is separated according to cloud pressure altitude based on the CO_2 slicing algorithm. The zonal distribution of the spectral forcing is a function of the cloud top altitude, and the effective cloud cover in the region. Thus, in the subtropical high regions the spectral forcing of the middle level clouds is nearly the same as for the high clouds. Regions of large amounts of convection have large spectral cloud forcing.
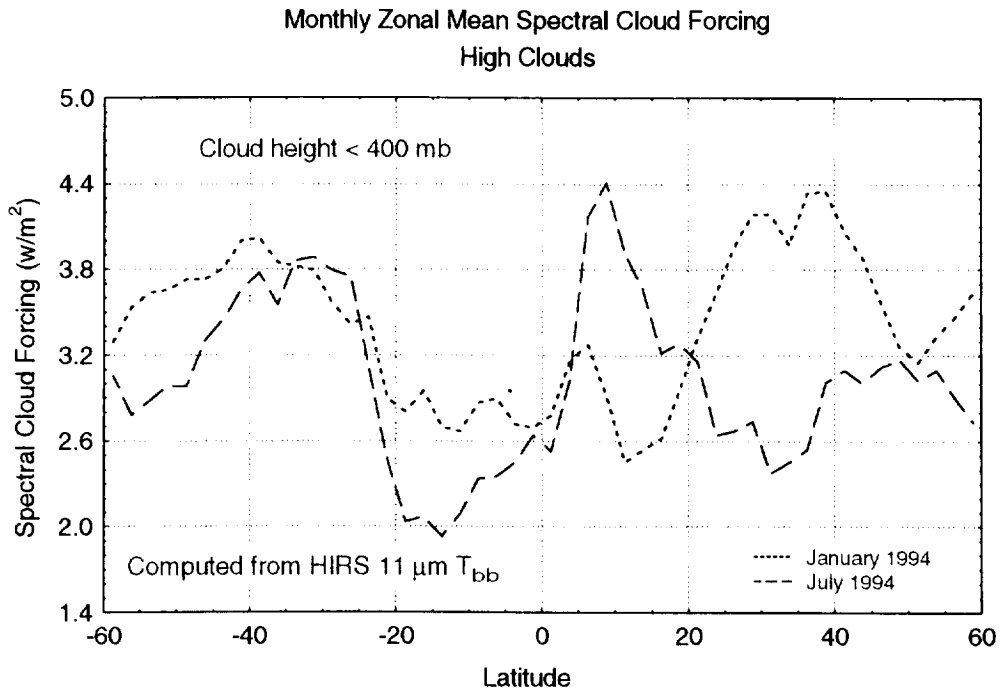
Monthly Zonal Mean Spectral Cloud Forcing
High Clouds

Figure 17. Zonal distribution of 11 μm spectral cloud forcing for January and July 1994, for cloud top pressure less than 400 mb.

26

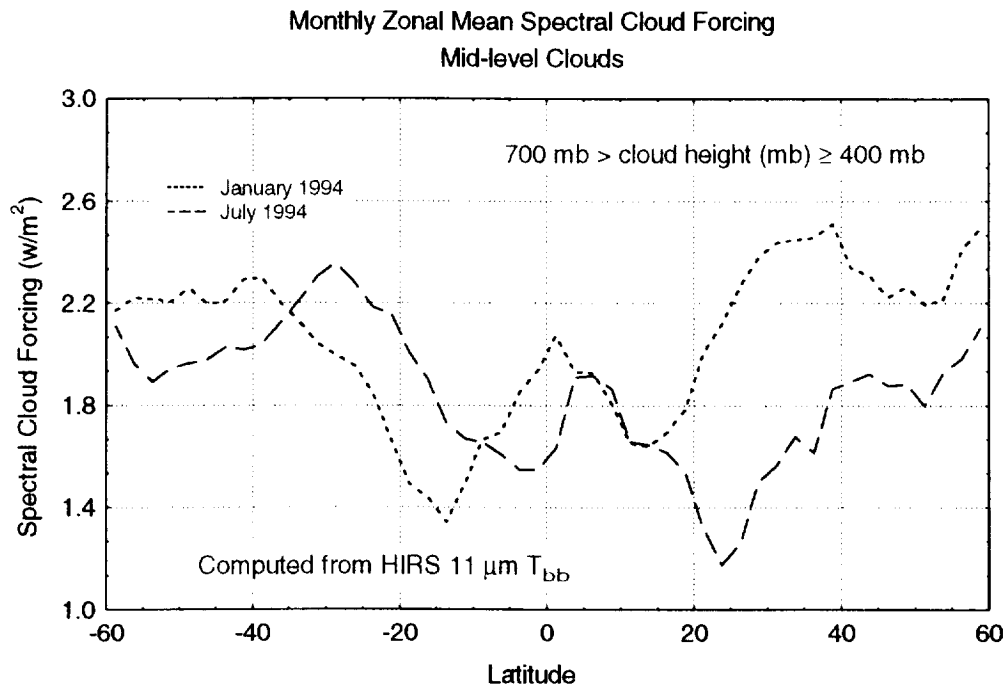Monthly Zonal Mean Spectral Cloud Forcing
Mid-level Clouds

Figure 18. Zonal distribution of 11 μm spectral cloud forcing for January and July 1994, for cloud top pressure between 400 and 700 mb.

27

Surface Properties

While clouds play an important role in modifying the radiative energy budgets at the top of atmosphere, variations can also be induced by changes in surface characteristics. To understand cloud radiative forcing over land and its interannual variability, we must also understand and distinguish the radiative forcing induced by changes in surface properties. Thus, we analyzed of the effect of changing surface conditions on the radiative energy budget through collocation of AVHRR observations within the ERBE footprint over the central United States. The surface condition is characterized through the Normalized Difference Vegetation Index (NDVI) and the thermal channel brightness temperatures. This required us to improve the cloud detection algorithm, which is briefly discussed below.

Cloud masking

A global cloud masking algorithm has been developed by the Cooperative Institute for Meteorological Satellite Studies (CIMSS) at the University of Wisconsin-Madison. The method uses radiance data from the Advanced Very High Resolution Radiometer (AVHRR) on board NOAA polar orbiting satellites at Global Area Coverage (GAC) spatial resolution (4 km at nadir). Use of collocated HIRS/2 data (17 km at nadir) is optional. In this study only AVHRR data is used in the cloud detection. A cloud mask value is determined for each individual AVHRR pixel in the region of interest, but information from surrounding pixels is sometimes used. For example, to ascertain the spatial continuity of a scene, the variance of radiance data may be computed from a block of pixels centered on the one of interest. This block (currently 3x3 pixels) of data is referred to as the "context" of the pixel. In addition, collocated HIRS/2 information from the upper troposphere is sometimes utilized (when available) even though it is representative of even larger regions.

The AVHRR algorithm is divided into eight conceptual domains according to surface type and solar illumination; daytime land surface, daytime water, nighttime land, nighttime water, daytime desert, nighttime desert, daytime and nighttime polar regions. "Daytime" is defined as a solar zenith angle < 85 ° while "polar" currently refers to any region poleward of 60° latitude. The "desert" classification is based on the 10-minute Olson World Ecosystems data. A USGS (United States Geological Survey) 1 km land/sea tag file is used for land/water discrimination. For all observations within a given domain, it is generally expected that: 1) the same tests may be performed, and 2) threshold values for each of these tests will not change. As yet, there are no sets of tests defined for nighttime polar or desert observations. The default nighttime land algorithm is substituted in both cases.

Once a pixel has been assigned to a particular domain, the spectral data corresponding to that location is subjected to a series of threshold tests designed to detect the presence of clouds in the instrument's field-of-view (FOV). These tests are the heart of the cloud mask algorithm. There are several types of tests, none of which are equally good at detecting all cloud conditions. For example, some are more reliable for low cloud or thin cirrus cloud detection, while others are better at finding any kind of optically thick cloud. Accordingly, tests which indicate similar cloud conditions are grouped together to obtain several intermediate results which are then combined to form a final cloud mask value. The tests are grouped so that independence between them is maximized. All tests that detect thin cirrus might make up a group, for example, while those which find high, cold clouds would form another, and low-level cloud

28

detection tests could make a third set. Of course, few if any spectral tests are completely independent of all the others.

Changes were made in the daytime land and desert subroutines. A problem was discovered with the fog and low cloud test over Olson World ecosystems 35 (corn and bean cropland) and 31 (crops and towns). Over these ecosystems the fog and low cloud test had a tendency to classify clear scenes as cloudy during the spring and summer. This was particularly true for the Southern Mississippi river valley. The solution to the problem was to not perform the fog and low cloud test over these two ecosystems.

The possibility of using NDVI values in a threshold test was also looked at for both land and desert areas. The NDVI threshold test was most successful at detecting clouds. Results of this test were very similar to the results of the visible threshold test. Clear sky NDVI values were often used in further studies of collocated ERBE and AVHRR data sets. In order to not introduce biases in these studies the NDVI threshold test was not used in the final cloud mask.

NDVI values did show some promise in detecting water related ecosystem problems. Under clear sky conditions NDVI values over continental areas are distinctly bimodal. NDVI values between -0.5 and -0.1 are due to inland water. The land processing path of the cloud mask could have been used over water areas for two reasons. Either because of changes in water levels have caused land areas to be submerged or mistakes in the collocation of the ecosystem map and the AVHRR data.

Surface effects on the TOA radiation budget

Our goal was to look at the effects of land surface properties on ERBE fluxes. To study these effects, we used the V-5 ERBE/AVHRR data files from March to October in 1985 (August was missing). All of which were from the NOAA - 9 platform. Since our ecosystem classification data set, Olson World Ecosystems WE1.4D, had higher resolution over the United States we started examining regions 626, 700 and 704. This gave us 18 images for each month. Unfortunately many of the region 626 and region 700 images were duplicates and some of the region 704 images covered very little land area. That left a seven month total of 35 days that had complete ERBE and AVHRR images. All of the months had data for five or six days except September which only had data for three days.

Ecosystem classification was accomplished using the Olson World Ecosystems. Of the clear sky AVHRR pixels in the 35 images that we looked at the seven most common ecosystems were (listed by order of most common):

51	Semi desert shrubs
41	Hot and mild grasses and shrubs
40	Cool grasses and shrubs
27	Conifer forest
26	Deciduous broadleaf forest
94	Crops, grasses and shrubs
22	Cool conifer forest

These seven ecosystems made up 67% of the clear sky pixels. Another 32% were the following 19 ecosystems (listed in order of Olson World ecosystem number):

2	Low sparse grassland
5	Deciduous broadleaf forest

7	Tall grasses and shrubs
8	Bare desert
11	Semi desert
23	Cool mixed forest
24	Mixed forest
25	Cool broadleaf forest
30	Cool crops and towns
35	Corn and bean cropland
37	Hot irrigated cropland
38	Cool irrigated cropland
43	Savanna (woods)
46	Mediterranean scrub
47	Dry woody scrub
55	Cool fields and woods
57	Cool forest and field
91	Woody savanna
92	Broadleaf crops

Histograms of NDVI values were analyzed for each of the 26 most prevalent ecosystems over the United States. As expected, desert like ecosystems had narrow ranges in NDVI values that were small yet positive while forest and crop type ecosystems had NDVI values closer to 0.5. Shrub and grassland type ecosystems fell somewhere in between. Inland water areas or flooded areas had NDVI values in the -0.1 to -0.5 range. An example histogram of monthly NDVI values is shown in Figure 19 for 3 different ecosystems: semi-desert, conifer forest, and cool grasses and shrubs. The NDVI histograms for March were often significantly different from those for the other six months for many of the ecosystems (see figure 19.b). The cause of this difference is likely due to changing snow cover. This may indicate that in March ecosystems may have different effects on fluxes than the same ecosystems during the summer and fall months.

An attempt to reduce the number of ecosystem being examined was made by calculating correlation coefficients between the NDVI histograms of all the different ecosystems for each of the seven months. Each ecosystem correlated quite well two or three other ecosystems, but none of them correlated well at all with another ecosystem for all of the seven months.
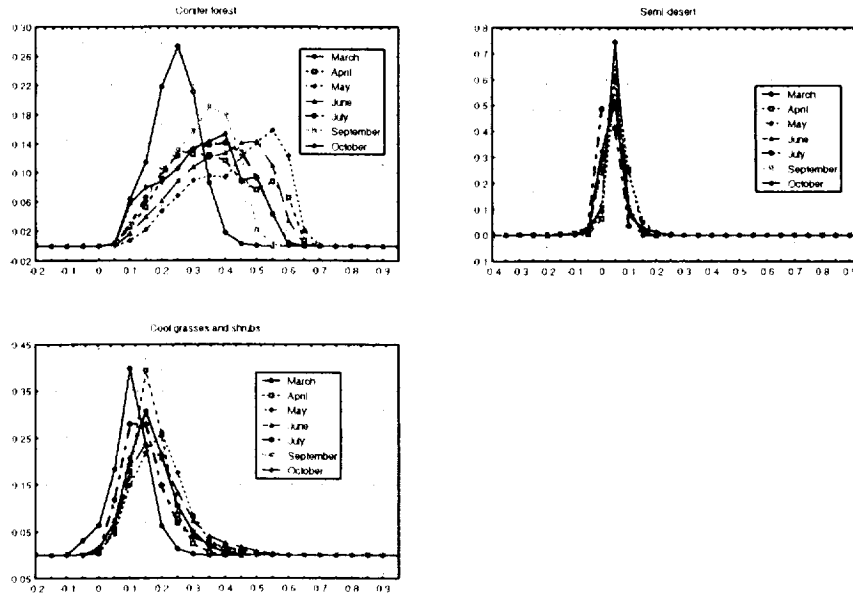
Figure 19. A histogram of the frequency of occurrence of an NDVI for 3 different ecosystem classifications.

Outgoing longwave radiation (OLR) and reflected SW for each of the 26 most common ecosystems depicted very little change in fluxes from one ecosystem to another. Figure 20 depicts the ERBE albedo versus NDVI as a function of ecosystem. Each point in the scatter plots is an ERBE flux where at least 80% of the footprint is the same ecosystem and the AVHRR pixels within the ERBE footprint have an average confidence clear value greater than 98%. As expected there is a strong dependence of NDVI on ecosystem. For high NDVI values (0.4-0.5) the variability of albedo for a given NDVI is a function of ecosystem. For example, compare the relationships between ecosystem 24 and 22.

Figure 21 displays a similar analysis for the ERBE OLR versus NDVI. As the NDVI decreases the ERBE OLR tends to increase. For a given NDVI, there is little dependence on ecosystem.
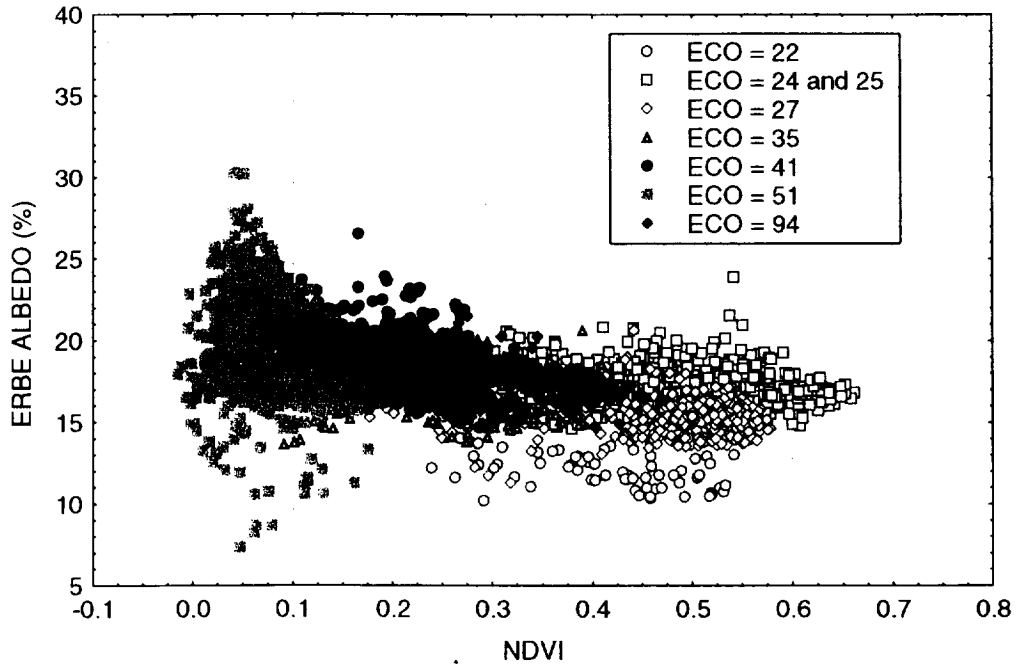
31

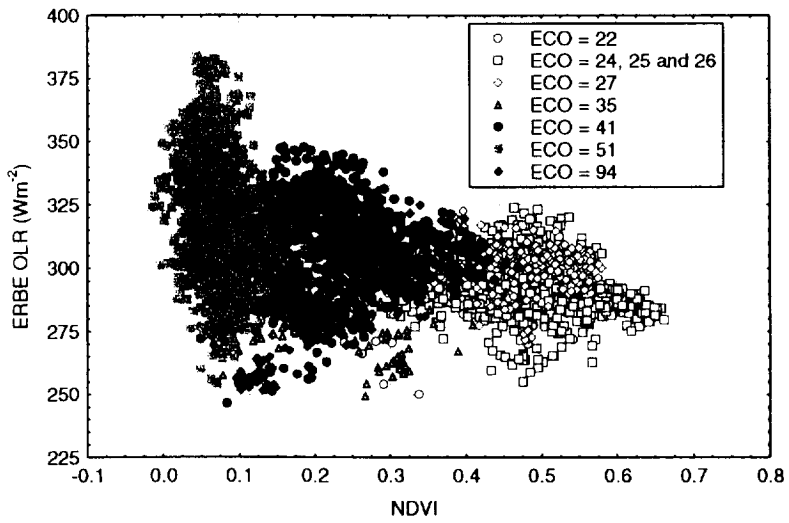Figure 20. ERBE albedo versus AVHRR derived NDVI as a function of ecosystem.

Figure 21. ERBE OLR versus AVHRR derived NDVI as a function of ecosystem.

Cloud forcing as a function of ecosystem was analyzed using ERBE pixels tha t contained at least 80% of an individual ecosystem. In order for an ERBE pixel to be considered clear-sky the clear-sky confidence value of the collocated AVHRR pixels had to be at least 98%. Unfortunately there were only a couple of ecosystems that had enough ERBE data to reliably calculate the amount of cloud forcing. The following table contains the results for these few ecosystems. Major differences in cloud forcing between ecosystems are larger for the LW than the SW. This generates a net cloud forcing that varies between -39 Wm^{-2} and -64 Wm^{-2}

Ecosystem number and type		Number		Cloud Forcing (Wm^{-2})		
		clear	cloudy	LW	SW	Net
26	Deciduous broadleaf forest	414	1346	-94	38	-56
27	Conifer forest	334	1244	-72	30	-42
51	Semi desert shrubs	1440	3464	-75	36	-39
94	Crops, grasses and shrubs	385	1163	-95	31	-64

33

The spatial and temporal variability of the earth's radiation budget.

The radiation budget observations from space are of great significance in studying climate and weather variability. They provide a global view of the sources and sinks of energy which govern the general circulation of the atmosphere and oceans. Interannual variations in the TOA radiation budgets are often assessed throughout and analysis of monthly mean variables. These differences are often small, except for years in which a significant change in the circulation of the atmosphere or ocean occurs, such as during an El Nino. Interannual variability can also be assess through analysis of monthly mean minima and maxima, modes, medians, or other statistical measures. This proposal investigated using other statistical measures for two regions of the globe, the continental United States and the Amazon.

Continental United States

To study the impact of using the mode of a distribution instead of the mean value, we analyzed NOAA-10 ERBE data for July 1987 and 1988. July 1988 was drought area from much of the Midwest and northwest. Figure 22 displays the mean values of outgoing longwave radiation (OLR) computed at a 1 x1 degree resolution grid. Legend on the right are in Wm^{-2}. Large difference between the two years occurs in the northern states of the midwest and west where 1988 OLR was greater by approximately 25-50 Wm^{-2}. The mean OLR values of the southwest have lower in 1988 than in 1987. Mean OLR is similar for the east coast.

The OLR mode values for the two months (Figure 23) are much larger than the mean values (Figure 24). Differences in the mode values between the two years tend to occur in the west. There is little difference in the mode values in the eastern US.
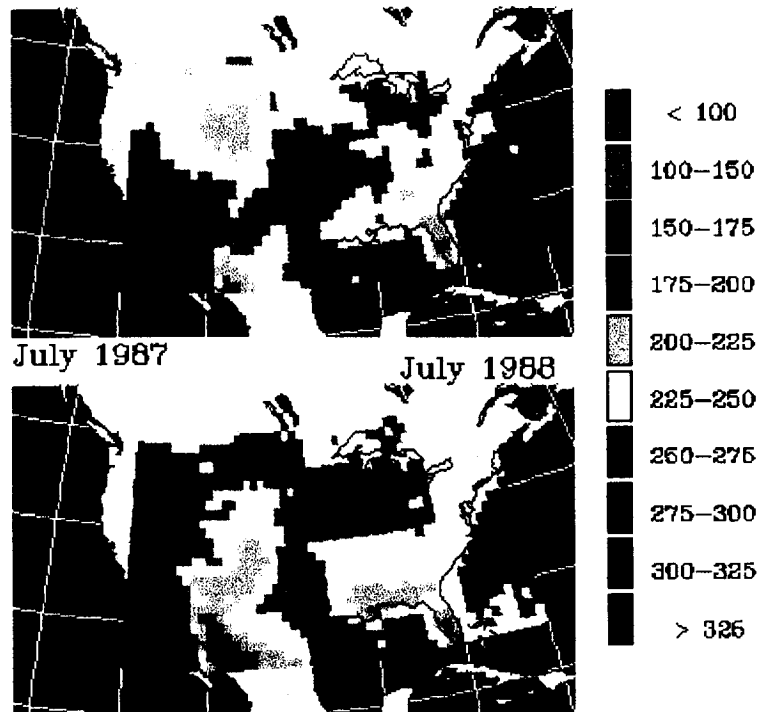
34

NOAA-10 Ascending Node Mean OLR

	< 100
	100-150
	150-175
	175-200
	200-225
	225-250
	250-275
	275-300
	300-325
	> 325

July 1987   July 1988

Figure 22. Mean OLR at 1 degree resolution for July 1987 and 1988 from NOAA-10

NOAA-10 Ascending Node Mode OLR

	< 100
	100-150
	150-175
	175-200
	200-225
	225-250
	250-275
	275-300
	300-325
	> 325
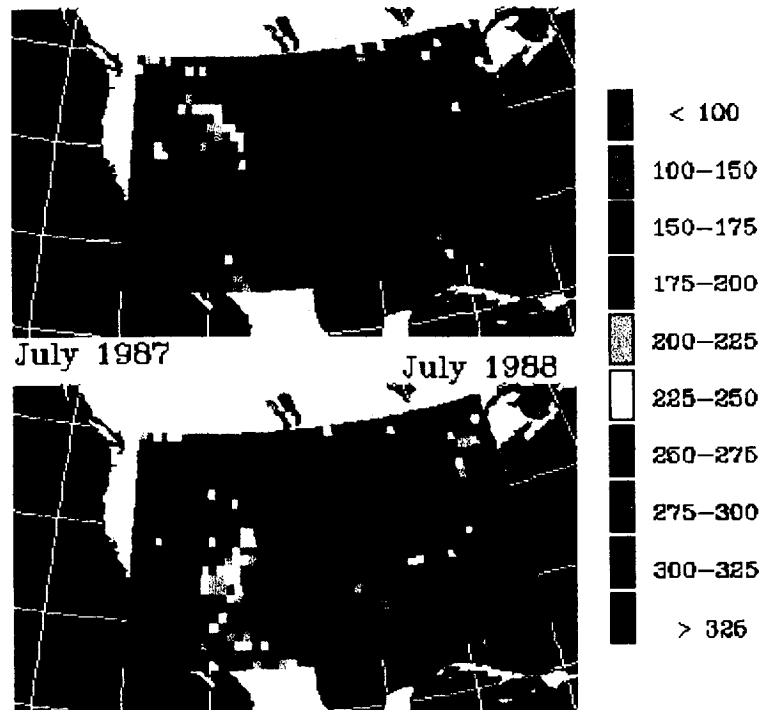
July 1987   July 1988

Figure 23. Mode OLR at 1 degree resolution for July 1987 and 1988 from NOAA-10
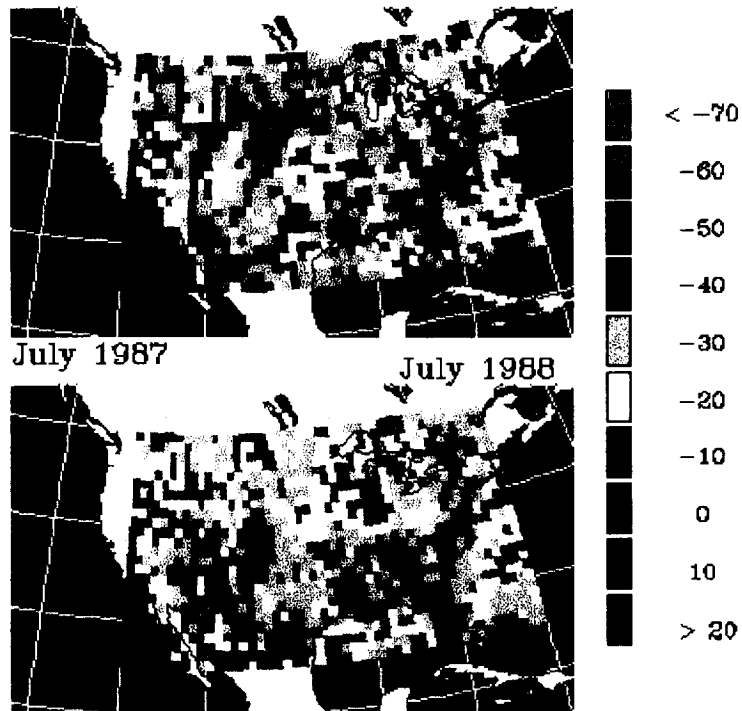
35

Figure 24. Mean-Mode OLR at 1 degree resolution for July 1987 and 1988.
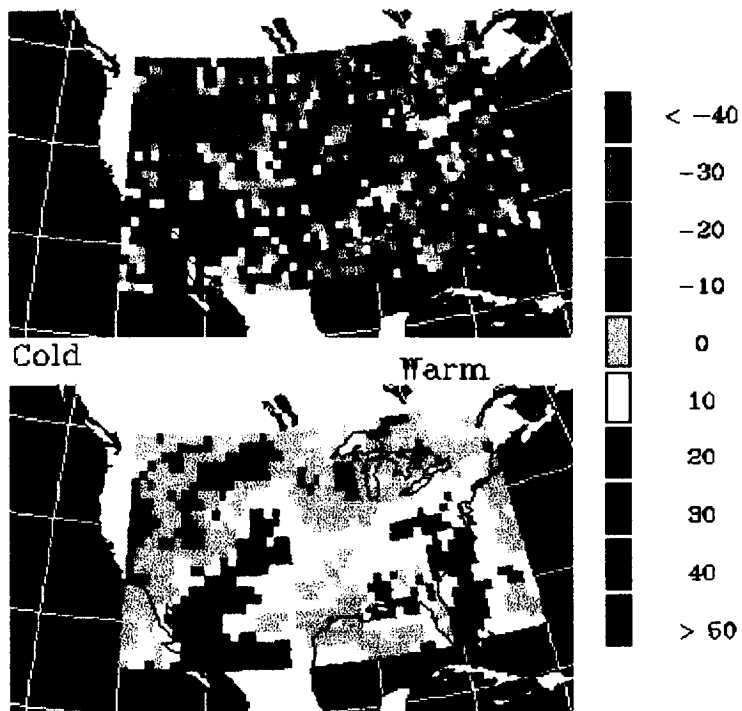
NOAA—10 Ascending Node 1987—1988

Figure 25. Difference between the coldest and warmest 10% values for July 1987 and 1988.

The coldest and warmest 10% of the data was also computed for the two months. Figure 25 displays the difference between these values for the two periods for the NOAA-10 ascending node. These maps help to interpret the differences observed in the mean value (Figure 22). For example, the upper midwest and west not only had more values of warmer OLR than 1987, but the 10% threshold for the coldest was much greater in 1988 than in 1987. The southwest regions mean values were lower in 1988. In 1987 the 10% warmest and 10% coldest values were both greater than in 1988. Also note, that while the mean values where similar for the east coast, there are differences in the upper 10% of the data and the lowest 10% of the data.

The α-trimmed mean was also computed for these two months. Defined as

$$x_\alpha = \frac{1}{n(1-2\alpha)}\left\{\left(\sum_{i=k+2}^{n-k-1} x_i\right) + (1+k-n\alpha)(x_{k+1} + x_{n-k})\right\}$$

if $k+2 \leq n\text{-}k\text{-}1$, otherwise

$$x_\alpha = 0.5(x_{k+1} + x_{n-k})$$

where $k=n\alpha$ is the largest integer $\leq n\alpha$ and $0 < \alpha < 0.5$, and x_i is ordered from smallest to largest. There was little difference between the mean and the α-trimmed mean.

37

Amazon

Research on diurnal variation in longwave fluxes at the top of the atmosphere for lands and ocean was conducted by Harrison et al., (1988, 1990) and Hartmann et al. (1991). These studies have provided insight into climate by illustrating the diurnal variation associated with cloud distributions and development at regional scales. In this study the effects of surface changes on the radiation budget at the top of the atmosphere were investigated by the analysis of upper quartile data in the dry season over the Amazon. By combining the collocated AVHRR data, the capability of the TOA fluxes from two satellites to detect changes in surface energy balance was also emphasized. The region of study is shown in Figure 26.
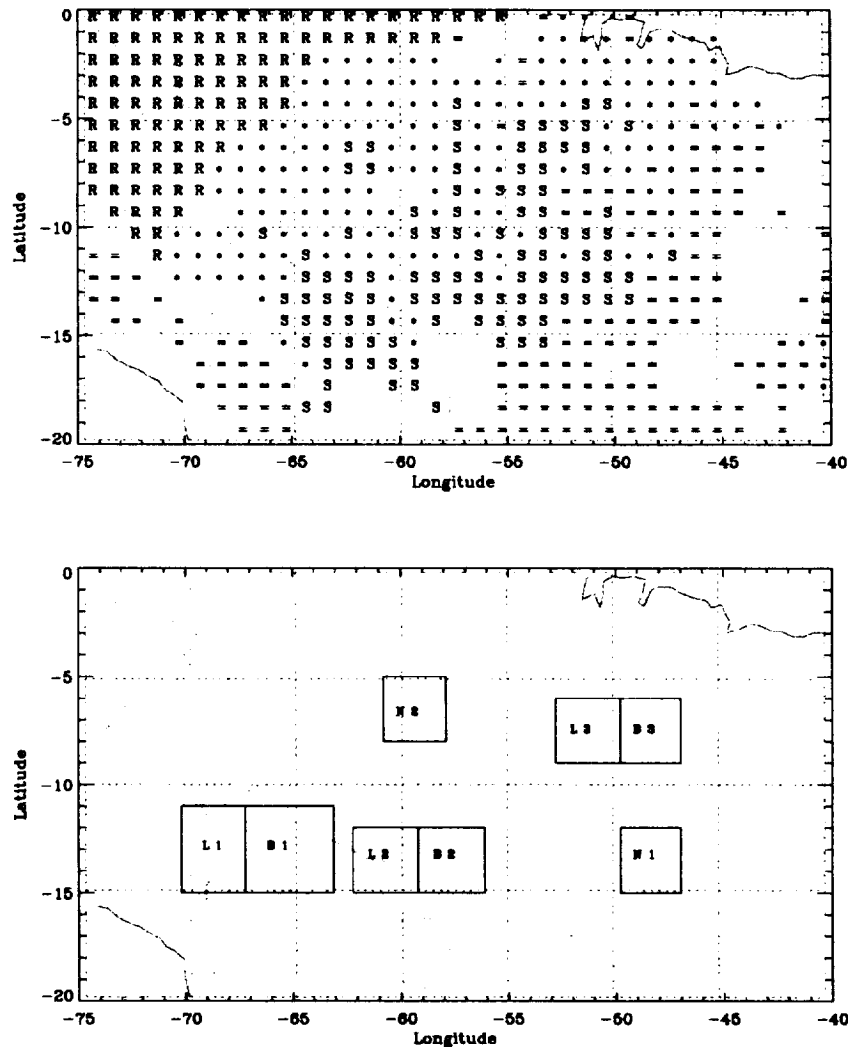
Figure 26. Region of study in the Amazon.

ERBE broadband top-of-atmosphere fluxes are used to study the energy budget as a function of surface condition. Since the intervening atmosphere and cloudiness can block the connection between surface and top-of-atmosphere energy balance, discernible surface radiative changes might not be detected in monthly statistical averages. In this study we made use of the upper quartile longwave radiation data (e.g. the strongest 25% of ordered outgoing longwave radiation), rather than analyzing mean values. The utilization of upper quartile data reduces the potential of cloud contamination in the top-of-atmosphere energy observation. Essential components of radiation diurnal variations including diurnal ranges and local times of diurnal extremes are also discussed in terms of upper quartile longwave measurements.

Two important parameters in radiation diurnal variability are the daily range and time of maximum and minimum. In this study, daily ranges are obtained by subtracting the diurnal minimum from the maximum for each 1 x1 degree geographic regions in the Amazon area. Two samples of observations are collected: one is composed of topmost 25% (upper quartile) observations, which is aimed at eliminating effects of cloudiness during a month and to demonstrate diurnal signatures over the clear-sky scene. The other contains the lowest 25% (lower quartile) data, which captures radiation diurnal changes affected by weather conditions including the amount and vertical distribution of clouds. Seasonal differences in diurnal variations are demonstrated using results from the dry month (August) and wet month (January), in which deep convective activities are common. Fluctuations of hourly observations in longwave radiation (LW), calculated using standard deviation, show the reliability of the monthly average diurnal signatures of ERBE TOA instantaneous observations. The second parameters investigated are local solar times (LST) of diurnal maxima and minima. These properties are used to explore detailed diurnal patterns suggested by previous studies.

Longwave Daily Range

The distribution of average diurnal ranges in LW flux during the five-year period (1985-1989) is illustrated for August in Figure 27. For most places in the Amazon, the LW diurnal range is between 50 and 90 Wm^{-2}. Some regions fluctuate more than 90 Wm^{-2} within a day, which is likely linked to cloud variability. An example is the tropical region between 0S and 5S shown in Figure 27. The average diurnal range is related not only to surface temperature variations but also to diurnal changes in cloud amount and types. However, if the warmest 25% LW (upper quartile) observations of the five year period are extracted it is shown that the diurnal variability reveals better clear-sky conditions. A smooth and consistent geographical distribution of diurnal ranges also suggests that cloud variabilities have been mostly eliminated. The daily range is generally less than 50 Wm^{-2}, which is typical for most land areas. Southwestern coast regions and part of the southern Amazon areas exhibit higher diurnal ranges (greater than 70 Wm^{-2}). Surface topography (such as mountain areas) and surface property (such as coarse savanna vegetation) account for the larger diurnal ranges, respectively. The diurnal range of the coldest 25% (lower quartile) LW data seems to suggest the effect of cloudiness, since the diurnal range increases to more than 110 Wm^{-2}. This may reflect that the cold cloud-top temperature decreases the daily minimum, thus increasing the diurnal range.
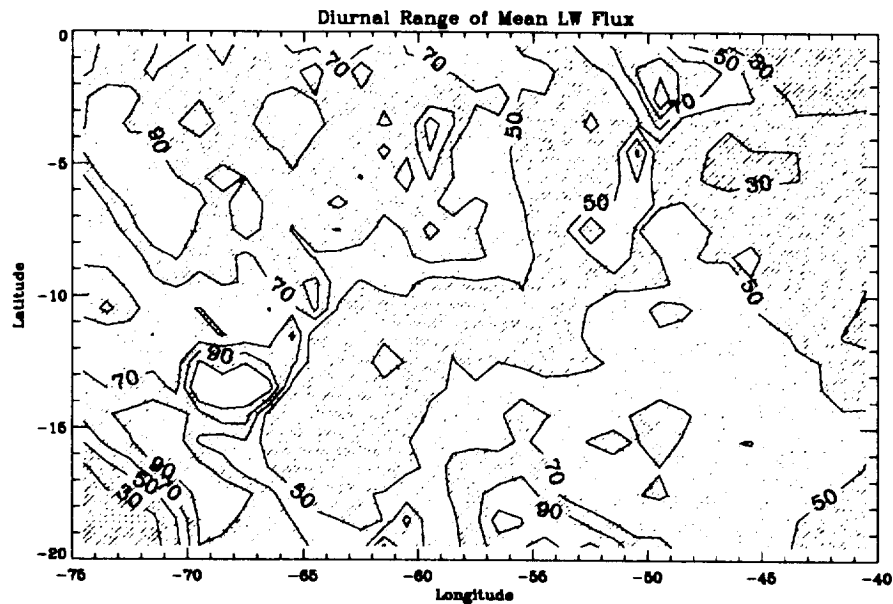
39

Figure 27. Diurnal range of the mean LW flux.

Times of Longwave Diurnal Maxima and Minima

Most radiation diurnal models applied to ERBE data are sinusoidal and symmetrical about local noon. The diurnal LW maxima occur near or before local noon with gradually decreasing values towards the times of sunrise and sunset. These studies relied upon theoretical half-sinusoid and linear interpolation. However, surface radiative budgets can deviate from this diurnal pattern. Through analysis of ERBE hourly observations, we seek to capture times of diurnal maxima and minima over several distinct regions of the Amazon. Five-year averaged times of diurnal maxima and minima are illustrated in Figure 28. The arrow points to a particular hour.

40

Northward pointing arrows indicate that the maximum (or minimum) LW radiation
occurs at 00 LST (midnight), eastward is 06 LST, southward is 12 LST and westward
is 18 LST. Mean diurnal signatures show that nearly 80% of the entire area exhibit
local noon or shortly before noon diurnal maxima (i.e. 11-12 LST). Northeastern parts
of the study region usually have mid-afternoon (15 LST) maxima. As for diurnal
minima, there is no fixed time interval for occurrences. Midnight minima are associated
with radiation cooling effects over land areas, while evening minima (18 LST) over the
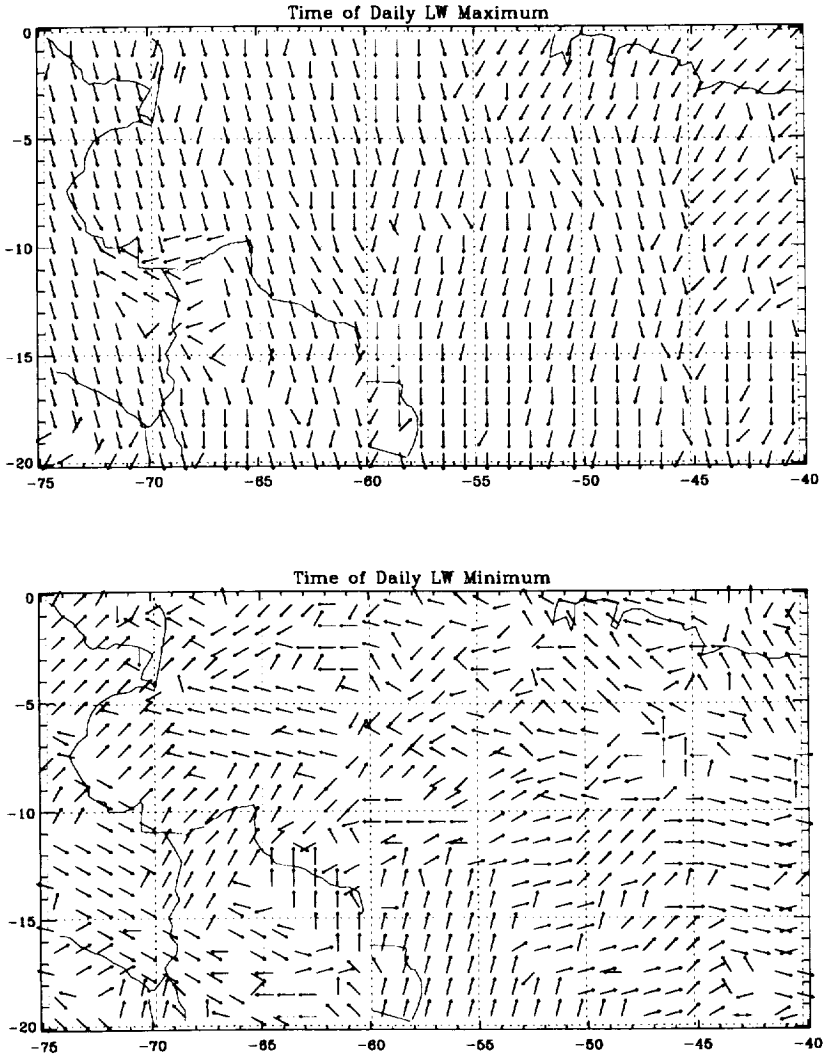tropical area seems to possibly be affected by clouds.

Figure 28. Time of daily LW maximum value.

41

Implications of Biomass Burning in 1988-89

Biomass burning comes from two sources: natural lightning and human activities. Rapid growth in the human population has caused biomass burning to increase. Most fires of human origin are related to agricultural activities. The location of burning is particularly prevalent between the tropics and subtropics and can be characterized into different vegetation fires. For example, in Africa, savanna fires are dominant while in South America both forest and savanna burning are frequent. The dry season is the most common time of a year for biomass burning.

Background Diurnal Variations of Non-Burned Regions

In South America, the deforestation rate is remarkably large: the estimate is 21,000 km^2/yr to 50,000 km^2/yr. Total burnt areas grow each year. Since burning is widespread in the tropical or subtropical regions, the effects on global atmospheric circulation are rather significant. Previous biomass burning research used an automated fire detection algorithm with GOES data and suggest there were a large number of active fires in the Amazon basin from late August extending to early September in 1988. The authors also detected less intensive burning for the same study area in 1989. In addition to estimates of burning areas, they noted that the diurnal signatures caused by burning are crucial for understanding fire activities. Since ERBE data provides adequate diurnal radiation information, it can be utilized to compare the differences in the diurnal variability of the TOA energy budget over burning areas and non-burnt surface regions. Based on results from Prins and Menzel (1994), there were two clean areas (refer to N1 and N2, respectively) chosen for our background study due to no burning activities observed over these areas. The associated ecosystems of these non-burned areas are grassland and broadleaf type, respectively. Locations of two non-burned and several other burned areas for this study are previously indicated in the lower panel of Figure 2.

Diurnal variations of LW flux over these two areas are shown in Figures 29 and 30. Results demonstrate that the variability over each area remains very comparable for both years. For example, area N1 has the LW peak at 15 LST in 1988. Although in 1989 it has larger fluctuations in hourly observations, there is still a tendency for increasing LW after local noon and the potential maximum is estimated at 14 LST. For area N2, the diurnal cycles are quite consistent for both years, but daily extremes are more difficult to define because of huge deviations in afternoon observations. It is also found there is less LW emission in 1989 than 1988 for both areas. The interannual difference is as large as 80 Wm^{-2}, but overall the hourly observations in 1989 are 30 Wm^{-2} less. The primary cause for the decreased LW in 1989 is due to the cold cloud top temperature. However, since the dry season (August) normally has fewer chances for developing deep convective activities than in the wet season, the substantial influence of cloud contamination obtained from upper quartile data is less likely. On the other hand, if convective complexes should exist, the diurnal variation would be completely different from those shown in Figures 29 and 30. Velasco and Fritsch (1987) showed that the LW variability under convective cloud conditions has very limited radiant emissions from evening until early morning, and that there is usually a maximum before local noon. As indicated in the current analysis, having the

42

comparable diurnal cycle from both years, it is impossible that cloud effects are exclusively found in 1989. Also, the diurnal cycles from the warmest 25% of radiation data do not possess diurnal properties coupled with convective activities studied by Velasco and Fritsch (1987). Thus the discrepancy rules out the argument for cloud influences in 1989. It is therefore suspected that the low surface temperature in 1989 caused less OLR detected from ERBE. Lower surface temperatures over the same area under clear-sky conditions is likely related to excess soil moisture whose evaporation buffered solar heating. The abundance of water content within the soil is mainly due to excessive rain in 1989.
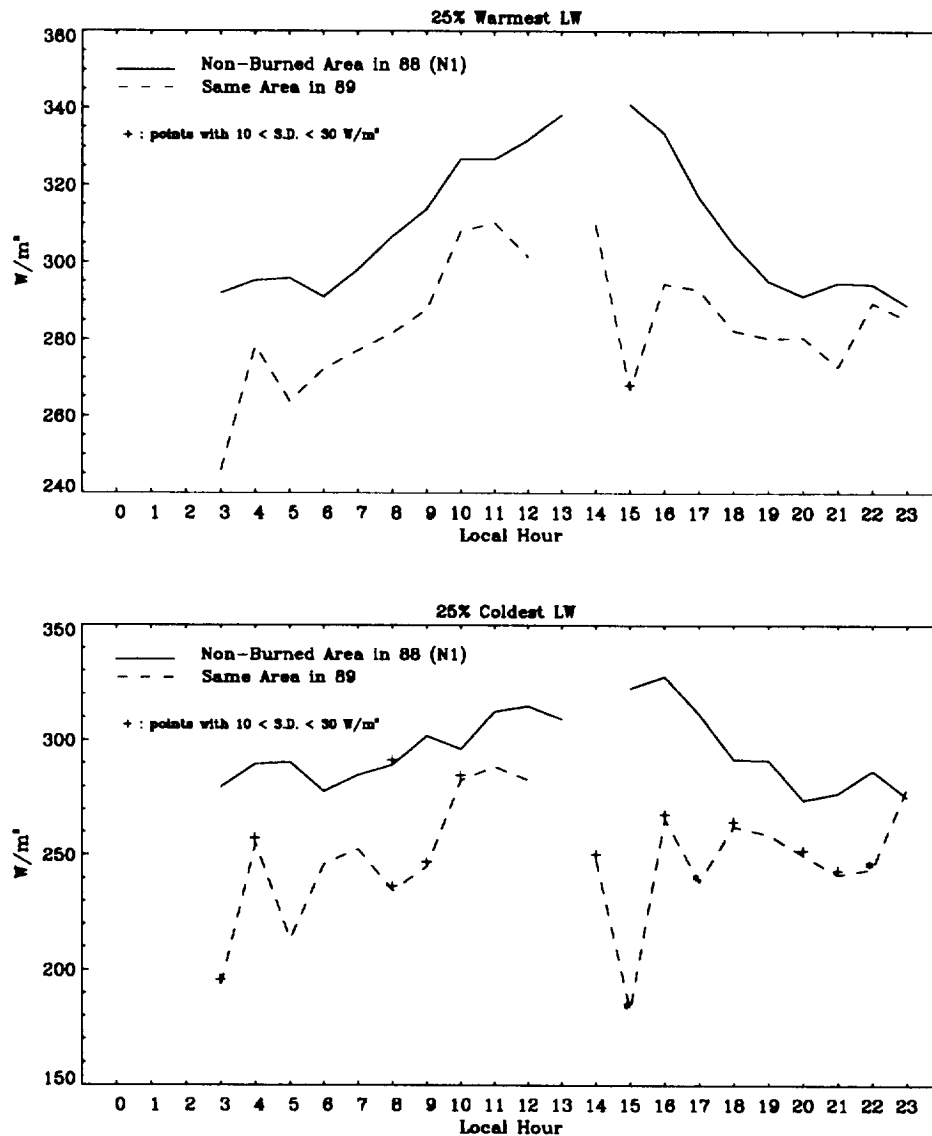

Figure 29. The diurnal variation of non-burned region labeled N1.
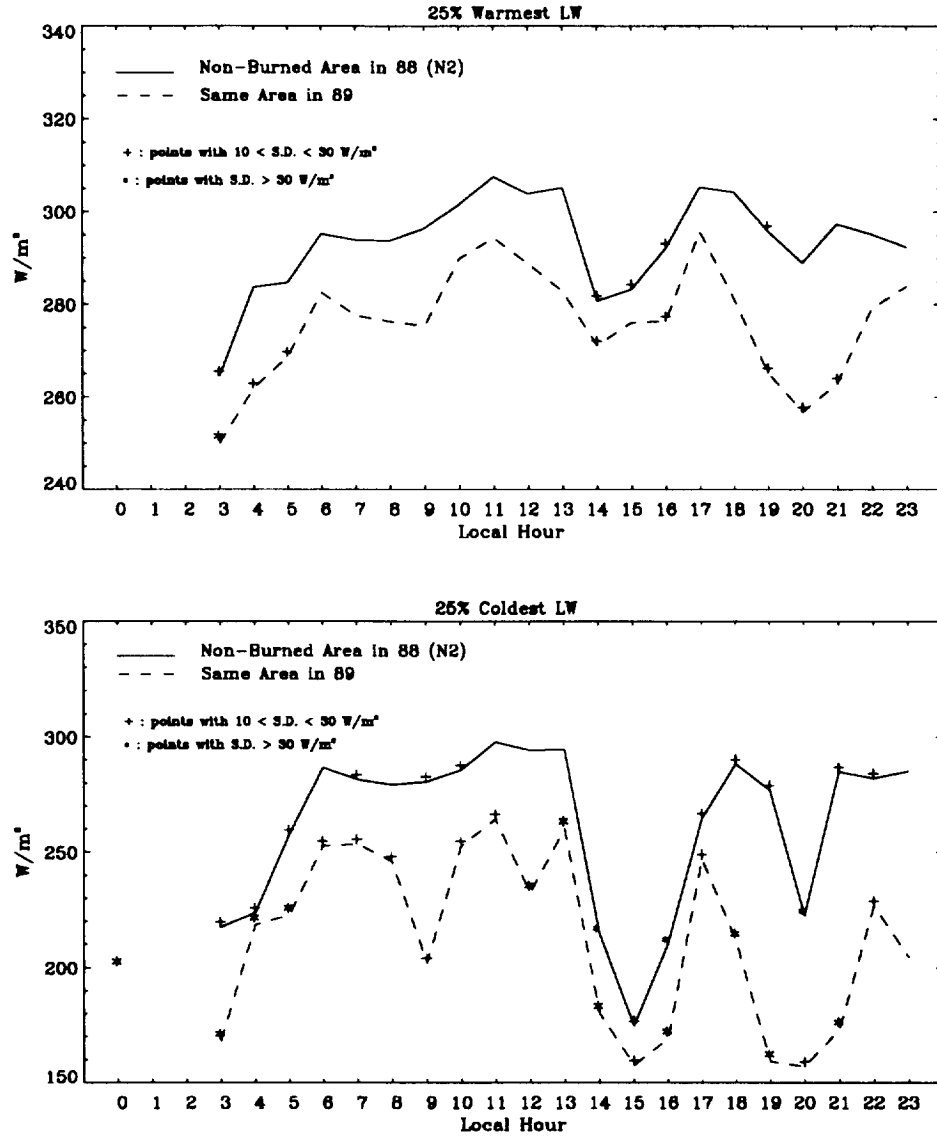
Figure 30. The diurnal variation of non-burned region labeled N2.

44

Burned Areas

Three areas with intensive burning detected in 1988 are selected to study the impact of burning on the energy budget at the top of atmosphere energy budget. For reference, less frequently burned areas adjacent to each burned area are also analyzed. The locations of those burned areas are referred to in the lower panel of Figure 26. Regarding the proportion of accumulated burnt areas for each burned area (B1, B2, and B3), area B1 represents the most intensive burned area detected in 1988, lesser burned areas (L1, L2, and L3) indicate at most, two third in 100-200 km $^{-2}$ of accumulated burning. In 1989, the burned areas (B1, B2, and B3) show different signatures from 1988. The burning intensity has reduced for each area. As for the underlying ecosystems, every area exhibits the various combination of surface vegetation. Area B1 has approximately 60% savanna and 40% tropical broadleaf. Area B2 is predominantly located in savanna region and area B3 is comprised of 80% tropical broadleaf and 20% grassland. The most intensive burning areas were categorized as cerrado fires, which may correspond to fire events over savanna regions. In each of three less significant burned areas, mixed ecosystems are shown as well.

The result of burning effects on radiation diurnal variations in the dry season for the warmest 25% LW radiation is shown in Figures 31, 32 and 33. It is seen that daytime LW emission over each burned area (B1, B2, and B3) is about 5 Wm $^{-2}$ more as compared to the contiguous, lesser burned areas (L1, L2, L3). LW maxima usually occur at mid-afternoon (around 15 LST) and the distinct LW emission (330 Wm $^{-2}$) is detected over burned areas. Lesser burned areas possess LW maxima close to local noon, such as 13 LST, and weaker diurnal LW maximum is detected (usually at 320 Wm $^{-2}$). Daily minima do not appear to be sensitive to burning for a given region. Areas with intensive or less burning both show LW minima before dawn. As for albedo variabilities, differences are not very noticeable. Albedo diurnal patterns are generally alike, and there are no consistent changes due to intense fires.

The figures discussed above also compare burn ed areas with the non-burned ones. Burned areas (B1 and B2) show weaker LW responses than non-burned area N1. Area B3 has somewhat stronger LW emission (about 10 Wm $^{-2}$) than N2. It appears that this comparison seems to be dependent upon which non-burned background areas we are analyzing as a reference. The inhomogeneity of ecosystems exists within each burned area, so the quantitative remarks about the differences in radiation variabilities between burned and non-burnt areas becomes difficult. Two non-burned areas (N1 and N2) represent the diurnal variations over rather homogeneous ecosystems (N1 indicates grassland, N2 indicates broadleaf), but all burned areas have mixed ecosystems, which adds to the complexity of a deeper investigation. Also, because many fires occur mainly over savanna areas, it is impossible to have clean and non-burnt savanna regions for comparison. Thus, the amount of modification due to burning is not easy to detect based one from the TOA broadband radiation measurements.

Although obtaining quantitative burning effects on the TOA radiative budget is difficult, the more intensive burning indeed shows a diurnal pattern with the more evident diurnal peak for the 25% warmest LW flux. The 25% coldest LW flux depicts relatively less comparable results due to more hourly fluctuations in observations. Also burned areas (B1 and B2) demonstrate more asymmetric albedo variations, with a

45

higher albedo (about 40%) at sunset or sunrise as compared to non-burned areas N1 and N2.

For the warmest 25% sample, the delayed time of diurnal maxima over burned areas are more evident in 1988 than 1989. In 1989, diurnal variations are less obvious even while fires are still active in area B2 (or B3). It is seen that LW emission is weaker in 1989 by about 20-50 Wm^{-2} less. The wetter surface conditions in 1989 induced by excess precipitation indeed disguised regular radiative characteristics, so the overall diurnal radiation variation is distinct from other years. For the coldest 25% sample, interannual LW energy differences are even larger (50-100 Wm^{-2} less in 1989). Albedo variations indicate that extreme high values occurring at sunset and throughout the afternoon from local noon to 16 LST are probably also linked to the natural variability in 1989.
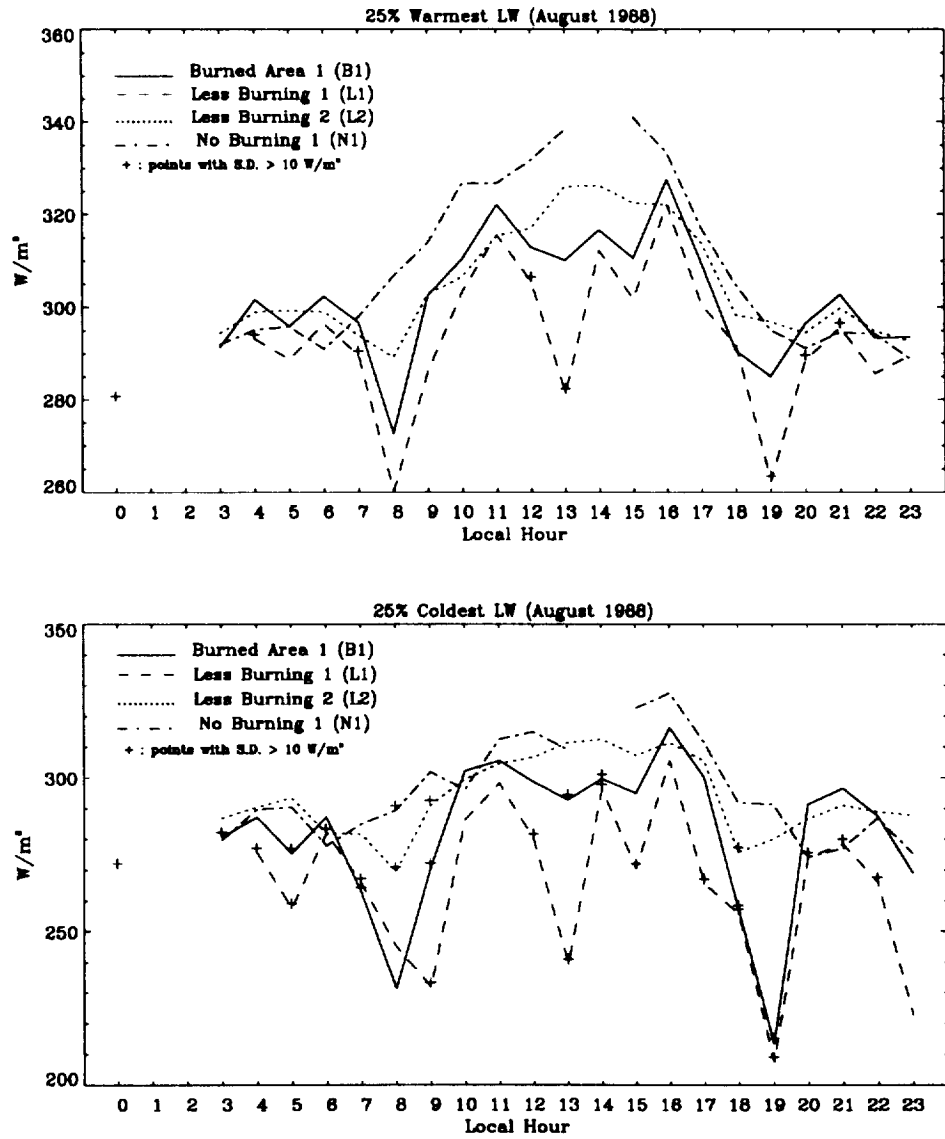
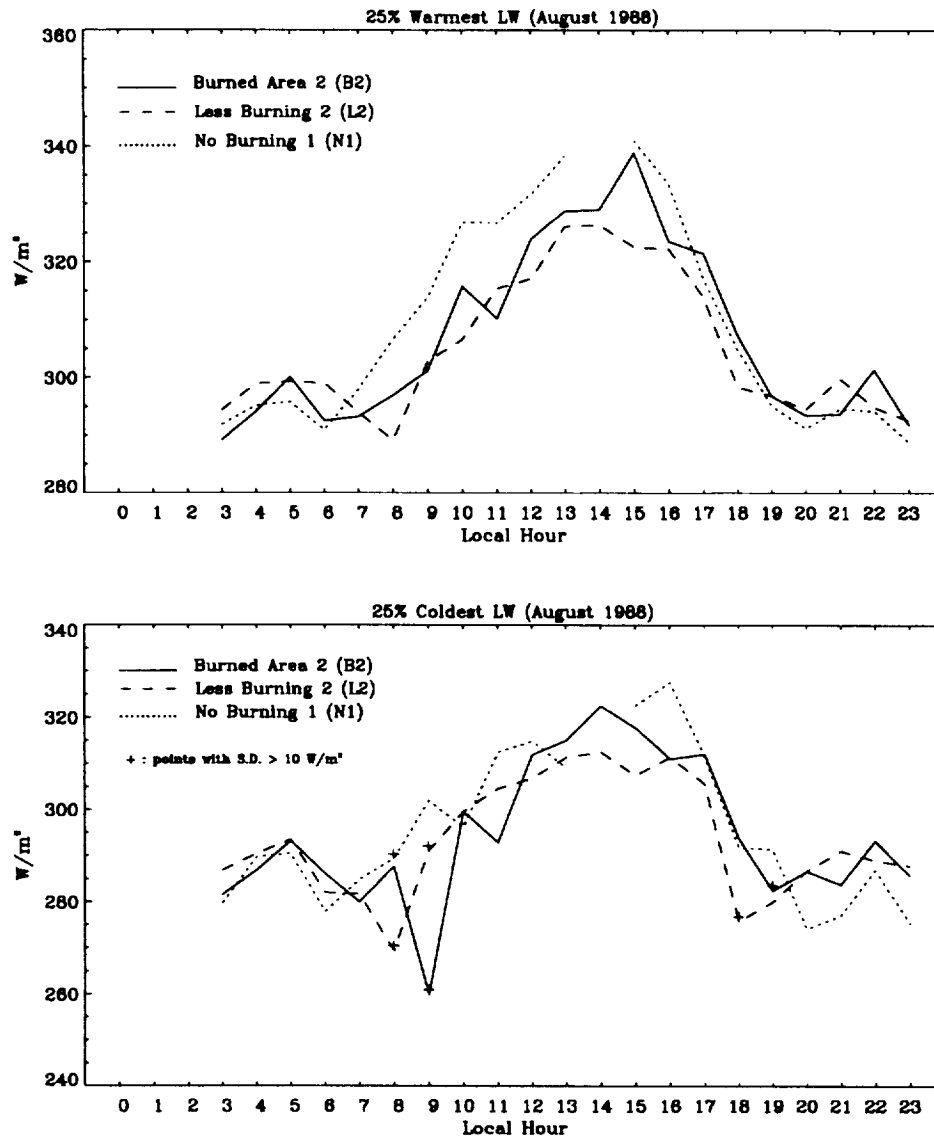Figure 31. The diurnal variation of burned region labeled B1.

47

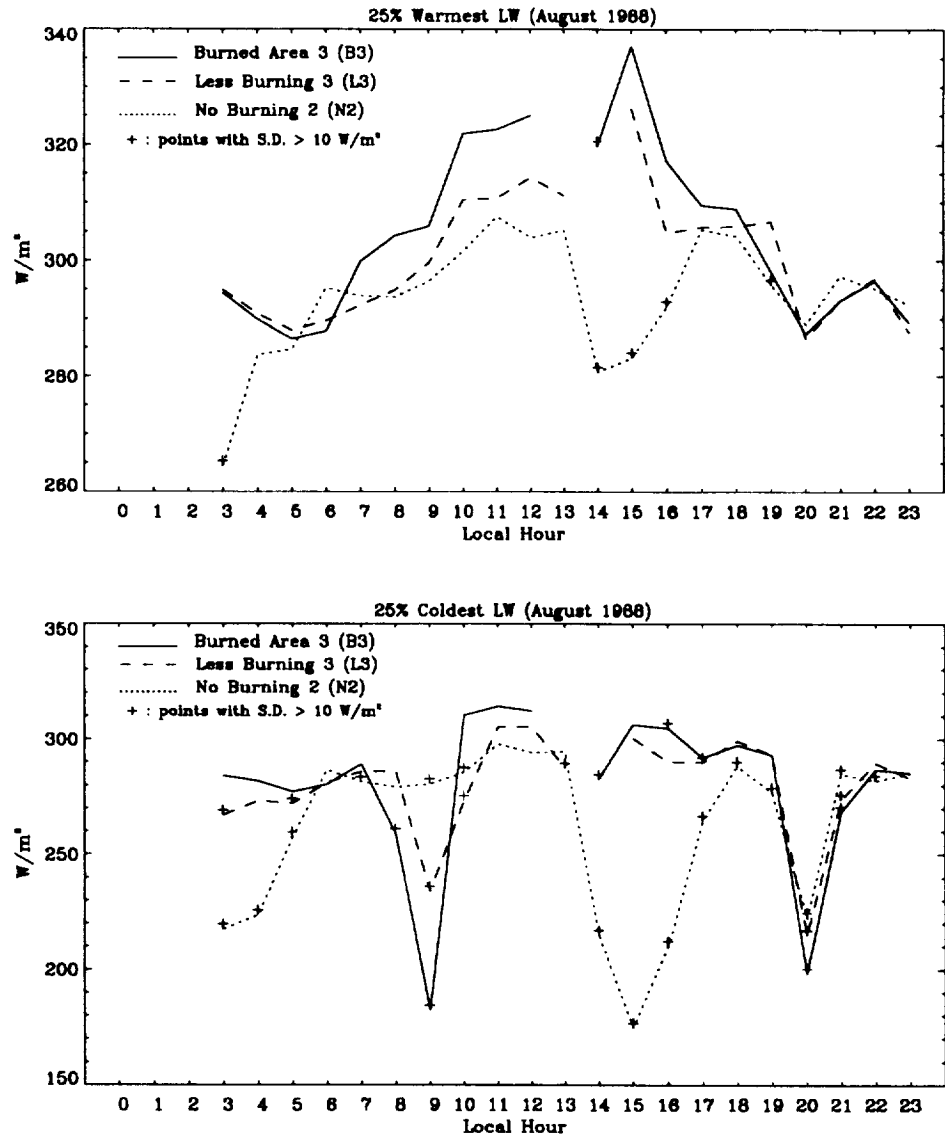Figure 32. The diurnal variation of burned region labeled B2.

Figure 33. The diurnal variation of burned region labeled B3.

49

The above findings in diurnal patterns affected by burni ng show the slight increase of LW energy (about 5 to 10 Wm $^{-2}$ more) and a delay in times of diurnal maxima till mid-afternoon for intensively burned areas. It is seen that the hotter surface and timing of biomass burning account for the change in the diurnal variation of the radiation budget. Albedo diurnal patterns are quite similar over areas with different levels of burning while burned areas tend to have an asymmetric diurnal cycle. Diurnal of patterns are more evident using the warmest 25% LW observations in August. However, the absolute radiation quantity affected by surface burning is not yet conclusive in this study. Interannual comparison indicates that burned areas have a decrease in LW emissions by about 20 to 50 Wm $^{-2}$ in 1989 which resulted mainly from natural wetness.

References

Ackerman, S. A., and T. Inoue, 1994: Radiation Energy Budget Studies using collocated AVHRR and ERBE observations, *Jour. Appl. Met.* 3, 370-378.

Ackerman, S. A., R. A. Frey and W. L. Smith, 1992: Radiation budget studies using collocated observations from AVHRR, HIRS/2 and ERBE instruments. *J. Geo. Res.*, 97, 11513-11525.

Barkstrom, B. R., E. F., Harrison, G. Smith, R. Green, J. Kebler, R. Cess and the ERBE Science Team, 1989: Earth Radiation Budget Experiment (ERBE) Archival and April 1985 results. *Bull Am. Meteorol. Soc.*, 70, 1254-1262.

Harrison, E. F., P. Minnis, B. R. Barkstrom, V. Ramanathan, R. D. Cess and G. G. Gibson, 1990: Seasonal variation of cloud radiative forcing derived from the Earth radiation budget experiment. *J. Geophys. Res.*, 95, 18687-18703.

Inoue, T., 1987: A cloud type classification with NOAA 7 split window measurements. *J. Geophys. Res.*, 92., 3991-4000.

Kopia, L. P., 1986: Earth radiation budget experiment scanner instruments, *J. Geophys. Res.*, 24, 400-406.

McClain, E. P., 1989: Global sea surface temperatures and cloud clearing for aerosol optical depth estimates, *Int. J. Remote Sensing*, 10, 763-769.

Ramanathan, V., R. D. Cess, E. F. Harrison. P. Minnis, B. R. Barkstrom, E. Ahmad, and D. Hartmann, 1989: Cloud-radiative forcing and climate: Results from the Earth radiation budget experiment, *Science*, 243, 57-63.

Smith, G. L., R. N. Green, E. Raschke, L. B. Avis, J. T. Suttles, B. A. Wielicki and R. Davies, 1986: Inversion methods for satellite studies of the Earth's radiation budget: Development of algorithms for the ERBE mission, *Rev. Geophys.*, 24, 407-421.

Stephens, G. L., 1990: On the relations between water vapor over the oceans and sea surface temperature, J. Clim., 3, 634-645.

Stephens, G. L. and T. J. Greenwald, 1991: The Earth's radiation budget and its relation to atmospheric hydrology, Part I: Observations of the clear sky greenhouse effect, *J. Geophys. Res.* 86, 15311-15324.

51